Effects of thermally-dependent rock parameters on fracture reactivation

Marius Meier

Master thesis in Applied and Computational Mathematics,
Institute of Mathematics,
University of Bergen,
Spring 2019

Acknowledgments

I would first like to thank my supervisors Michele Starnoni and Inga Berre who made it possible for me to complete this thesis. Especially Michele, for the countless hours he helped me beyond what was required of him, and the patience he had with me. Furthermore, I would like to thank Runar Lie Berge who helped me when I had problems even though he had no obligation to do so. I would like to thank Bolla who cared and believed in me, and put up with my frustrations. I would also like to thank everyone at kontoret who made it extra fun to study, and my friends outside of academics who made life awesome. Lastly I would like to thank my family who gave me encouragement.

Abstract

The slip tendency is an important tool to measure fracture reactivation in the context of subsurface engineering applications. In this thesis, the effects of thermally-dependent rock parameters such as Young's modulus on the slip tendency are examined by running several two-dimensional simulations in a porous media with a single fracture. The numerical solver used is the MPSA method which is a modified finite volume method used for elasticity problems. First, simulations are done with two different sets of boundary conditions to see which combination of boundary conditions and fracture orientation produces the highest slip tendencies. After the best combination is found, the simulations are done again with varying temperature to see the effect temperature has on the slip tendency. A third series of simulations follow with a temperature gradient acting on the domain which is dependent on the depth of the domain. All the simulation results represented here clearly indicate that temperature variations, varying orientation of the fracture and varying Young's modulus on the surrounding matrix as a function of the temperature have significant impact on the slip tendency.

Contents

1 Introduction

1.1 Background on applications for thermal deformation

The understanding of how fractured rocks behave under temperature fluctuations in the subsurface is an important, and interesting field because of its broad application. It is for instance needed in deep storage of nuclear waste, carbon capture and storage, underground coal gasification, the development of infrastructure of underground cities and in geothermal energy. Understanding the thermal effects on rocks also helps to better understand many processes which takes place in the earth's crust such as heat transport, fluid flow, deformations etc.
Since the development of geoengineering in the 1970s a number of studies involving temperature, fluid effects and mechanical stresses have been done to better understand the influences they have on the mechanisms happening within a porous media. This has later resulted in several coupled thermo-hydro-mechanical (THM) simulation models in fractured porous media simulating a variety of processes [Weizhong et al.2009].

Being able to simulate the coupled processes taking place for rocks in the subsurface requires a solid understanding of the interconnected processes. It is a complex coupling of the pore fluid pressure, the thermal effects, and the macroscopic stresses on the rock. These processes depend on the type and state of the rock formations, in situ conditions on the stresses, temperatures, pressures and the composition and nature of the pore fluid phases.

There has been done various simulations of coupled THM processes in subsurface rocks as it is important in a number of engineering applications. The rise in computational power and more robust algorithms has made it more convenient to complement field simulations with computational methods, and theoretical approaches. Field simulations are often costly and risky, and so available data will often be limited. Furthermore, most projects need to measure different operational scenarios on far larger spatial and temporal scales than what can be done with direct measurements. It is also the case that simulations are needed in high impact, low probability scenarios as simulations will be too risky. For instance in leakage from nuclear waste repositories or induced seismicity due to large scale fluid withdrawal/injections [Kelkar et al.2014].

The standard structure is to first develop a mathematical model, which consists of defining the domain, the governing equations and the boundary conditions of the problem. In general, some simplifications and assumptions are made on the properties of the rock, fluid, fractures etc., followed by defining the constitutive and governing equations for the stress and strain, heat and fluid flow, mass and energy equations etc. Finally, to solve the problem at hand, a numerical model based on a discretization of the governing equations is used.

Since the interplay of the processes in fractured porous media are highly complex, simplifications are commonly made, there are several, for instance leaving out permeability-stress

relationships, temperature gradient effects on fluid flow, having non-deformable or unsaturated porous media etc. [Weizhong et al.2009].

This thesis will look at a thermo-mechanical relationship. Specifically how temperature affects certain thermally dependent rock parameters and how this in turn will affect the slip tendencies of fractures.

1.2 Aims of research

The following objectives are proposed for this thesis:

- to increase understanding of temperature effects on thermally dependent rock parameters
- to provide more insight on flow and mechanics
- to provide insight into the relationship and correlation between temperature and slip tendency

As part of the thesis, an additional aim is to get accustomed to to using Porepy, a simulation tool for fractured and porous media. Porepy will be used as a simulation aid in the topic of understanding the influence temperature has on thermally dependent rock parameters and in turn how it affects the slip tendencies of fractures in rocks. Specifically the temperature effect on Young's modulus E will be an important factor.

Although there is some research on the topic of slip tendency, the effect temperature has on the slip tendency is rarely discussed. The research that does look into it often have several factors which may affect the slip tendency. This results in not knowing which processes actually affect the slip and to what degree.

Porepy is the program that has been used in this thesis to simulate the simulations. Porepy is a simulation tool for fractured and deformable porous media written in python by the porous media group at the University of Bergen. The structure of the rock is simulated as either standard 2d and 3d grids or mixed-dimensional grids defined by intersecting fracture networks. Porepy can be used for visualization and analysis of fractured domains as well as discretization of flow, transport, elasticity and poro-elasticity using the finite volume and virtual finite element methods Keilegavlen [Keilegavlen et al.2017].
Porepy can be found at: "https://github.com/pmgbergen/porepy".

1.3 Outline of Thesis

This thesis will look at the effects thermo-mechanical coupling induces on the slip tendencies of fractures. The thesis is organized as follows, it will start with introducing the background on THM simulations in Ch. 2, followed by covering the basic framework which is needed to understand the research. That is, explaining some governing and constitutive

laws which are needed in rock mechanics followed by a small topic within fracture mechanics. Furthermore, friction and slip tendency is introduced followed by temperature dependent relationships and lastly a model of the problem in Ch. 3. The numerical models which are used to solve the relevant equations are explained in Ch. 4. Lastly, the simulations and results of the simulations are shown in Ch. 5, before finally ending, with a conclusion of the simulations and the thesis as a whole in Ch. 6.

2 Background on THM simulations

2.1 Examples of general THM simulations

Some examples of THM coupling is found for instance in [Khalili and Selvadurai2003] who made a fully coupled constitutive model for THM analysis in elastic media with double porosity. The model was made of three separate yet interconnected models consisting of deformation, flow and heat transfer. The deformation model was based on the theory of thermoelasticity, the effective stress concept and the equations of equilibrium. The flow model was based on the double porosity concept and two interacting mediums were identified: One representing the porous blocks and one representing the network of fissure. The two regions were connected through a leakage term describing the fluid transfer from the porous block to the network of fissure and vice versa. Finally the heat transfer model was based on the assumption of thermal non equilibrium between the phases. The modes of heat transfer were assumed to be conduction, advection and heat exchange. The article showed that the development of the equations governing THM processes in elastic media with double porosity could be approached in a systematic manner where all the constitutive equations governing fluid flow, deformation and heat transfer could be combined with the conservation laws.

[Bower and Zyvoloski1997] made a numerical model for THM coupling in fractured rock. There are several approaches to solve the THM couplings. One of them is the fully explicit approach in which all the conservation equations are treated explicitly in time. Here the non-linear terms are evaluated at the previous time step and are easily accounted for. The time steps in the explicit approach are very small.

Another approach solves each conservation equation implicitly, but updates the coupling terms in a sequential manner. The advantage here is that the method is not limited by small time steps, but the convergence rate will be dependent on the magnitude of the changes in the coupling terms.

[Kelkar et al.2014] has developed a THM simulator in a single integrated control volume finite element code named FEHM, with the option of solving a THM problem using either implicit or explicit coupling. it is been developed to address problems for heat and fluid mass transfer in the subsurface. [Bower and Zyvoloski1997] made modifications to FEHM so it could be used for hydraulic and thermal coupling, hydraulic and mechanical coupling, and hydraulic, thermal and mechanical couplings.

[Salimzadeh et al.2018] made a fully coupled THM model that rigorously models deformable fractures in a permeable matrix. The model was constructed from five separate yet interacting sub models. A thermoelastic deformation model, two flow models and two heat transfer models where one was for the flow and heat transfer in the fracture and one for the rock matrix. The governing equations were solved numerically using the finite element method while the galerkin method and the finite difference techniques were used for spatial and temporal discretisation respectively. The THM model was further coupled with

a contact model to resolve the contact stresses between fracture surfaces. The model was applied to several geothermal systems in both impermeable and permeable rocks.

Another important aspect is an uncertainty analysis of the numerics of THM simulations, which is important in order to get more insight into how reliable THM simulations actually are. Data is one of the major uncertainties in subsurface reservoirs due to the limited measurements because of the costs and technical issues. Subsurface data is gathered from a small sample size so the subsurface models are derived from limited information and carry a certain uncertainty. [Watanabe et al.2009] made a stochastic uncertainty model for a hot dry rock (HDR) geothermal reservoir. The majority of the data base for the study came from recent and former German HDR projects at Urach Spa, which has a highly fractured reservoir in crystalline rocks.
The statistical approach for the uncertainty analysis consisted of three parts: 1. determination of statistical models for spatial distribution of physical rock parameters. 2. stochastic realizations of parameter fields using conditional Gaussian simulation based on the defined stochastic models. 3. Monte Carlo analysis with numerical simulation of fully coupled THM processes using randomly generalized multiple parameter distributions.

The stochastic model created was a combination of a coupled THM model and a Monte-Carlo method. There were several assumptions for the stochastic model used, and two of them were that the parameters of THM processes were considered as spatial random variables and the parameter distributions had spatial correlation as well as heterogeneity over the reservoir.
Sensitivity analysis shows that permeability and rock specific heat capacity are the most important reservoir parameters. Accounting for variable fluid properties is very important with THM analysis and the most sensitive parameter is the fluid viscosity. The maximum temperature uncertainty range found was of about 40℃ after 15 years of reservoir exploitation.
The major drawback with the model was the exclusion of fractures since it was not enough data available in the Urach site to justify a discrete fracture network model.

2.2 Examples of slip tendency analysis and fracture reactivation

For this thesis it is the thermo-mechanical coupling that is most relevant, specifically calculating the slip tendency to know the likelihood of fracture reactivation. As such, a few articles based on the topic of slip tendency will be discussed to further motivate the problem.

In the beginning the use of advanced numerical methods was not a great option for fracture reactivation analysis due to the methods being too complex or time consuming in terms of both computation and preparation. Several methods were developed to predict fracture behaviour in tectonic stress fields prior to numerical methods. One of them was a graphical approach with the use of Mohr's circle [Jaeger et al.2007], while another one was an analytical approach by [Sibson1985]. The usefulness of these methods is that they are quick, simple and some of them can handle a large number of fractures simultane-

ously. All of these methods are based on the Wallace-Bott hypothesis which states that the most likely orientation for a fault to slip is parallel to the direction of the maximum resolved shear stress. An interesting paper discussing slip tendency and its application is for instance [Morris et al.1996] who was the first to make a slip tendency analysis in 1996 and made it for assessing relative risk of earth quakes and fault slip. An interactive computer tool was made which displayed the stress tensor in terms of its associated slip tendency distribution and the relative likelihood and direction of slip to occur in terms of all possible surface orientations. The surfaces were oriented arbitrarily within a stress field to be able to compute the slip tendency for all surfaces of every orientation. The principal stresses could also be modified to see how it affected the slip tendency on an individual surface. This procedure was applied to mapped fault traces to investigate the various stress fields on known or suspected faults at the Yucca mountain in Nevada. The study concluded that the key uncertainty in predicting which faults were to slip in the Yucca mountain was the orientation of σ_3.

[Worum et al.2004] made a numerical approach applied to three dimensional fault models to calculate the slip tendency in order to constrain fault reactivation. 3-D geometrical fault models in combination with assumptions on the tectonic stresses around faults were used to calculate first order approximations of the normal and shear stresses at every location of the faults. The patterns of slip tendency and shear direction approximated provided useful three dimensional constraints about the likelihood and style of fault reactivation. The model was used to predict fault reactivation for the Roer Valley Rift in the Netherlands. The model was based on a three step procedure. During the first phase the 3-D geometrical model of the fault pattern was prepared and the confining stress field was determined. The model was represented by triangulated surfaces generated by a software package named GOCAD. The second step involved calculating the magnitude of the contact stresses, the direction of the shear stresses and the slip tendency with the use of a Java2 computer tool. The last step of the numerical analysis was the evaluation of the computed parameters. The software GOCAD was also used for this process which resolved the stresses in order to constrain the reactivation pattern of the faults.

[Moeck et al.2009] used a slip tendency analysis to predict fault reactivation and induced seismicity in a deep geothermal reservoir. Geothermal systems are often stimulated by hydraulically induced fractures to increase the productivity. A slip tendency analysis is therefore essential to predict fault reactivation potential and to mitigate undesired high seismicity. The study was done in an enhanced geothermal system of the Northeast German Basin in 2007 and the slip tendency method was used to characterize fault slip likelihood and slip directions in a geothermal reservoir. The results from the slip tendency analysis combined with geomechanical parameters showed a low likelihood of slip to occur in the volcanic succession of the reservoir. This indicated that high additional fluid pressure was needed to reactivate the strike slip or the normal faults. The study had water injected into the volcanic rocks of the reservoir during a 6 day period which ended with a surprisingly low level of seismicity near a presumed normal fault. The fluid pressure was increased from 43 to 86 MPa. The first failure occured with 20 MPa additional fluid pressure whereas the slip tendency analysis predicted it to occur after 24.5 MPa. The error could either be explained by error bounds or a high degree of fracturing of the volcanic

rocks located near the reactivated fault. However the low magnitude of seismicity recorded during stimulation was consistent with the results from the slip tendency analysis. The study therefore concluded that a slip tendency analysis is a reliable method to characterize, investigate and understand the faulting behaviour of engineered sub-surface reservoirs.

[Neves et al.2009] coupled slip tendency analysis with a software named COULOMB to visualize slip tendency on faults in 3-D which is an improvement to the 2-D visualization of [Morris et al.1996]. COULOMB is a popular software for deformation and stress change used in earthquake, tectonic and volcanic research.

For predicting and visualizing the slip tendency the COULOMB software takes in four input arguments. The principal stress directions, the stress difference ratio R, the friction coefficient μ and the geometry of the fault system. The program can analyze tens of faults in a very short time and returns graphical results. However, some requirements are needed in the sense that the stress field needs to be homogeneous and the faults are assumed to be planar with no interaction between each other. A few of the program's functions are for instance computing the slip tendency for all faults and plotting a 3D view of the fault planes showing the the slip tendency in a code colored scale. Another one is the ability to compute the slip tendency for all faults and display the ones with a slip tendency greater than 0.5 as a dashed line in a 2-D grid drawing. There are several other functions to the software and it was used to study the Horseshoe region in the Gulf of Cadiz.

In summary, there are several THM models and numerical methods that solves for coupled THM processes. Yet, most slip tendency analyses are mostly concerned with the mechanical parts and some on the hydraulic processes, but very little on the thermal effects. This is reasonable in the sense that the mechanical and hydraulic processes will most likely have the greatest impact on the slip tendency. Yet, neglecting temperature effects on the thermally dependent properties of rocks may cause an error in the computed vs actual slip tendency values. This remains to be seen and will be explored in the thesis, but first an explanation of the theory is needed.

3 Principles of Rock Mechanics

There are two fields in the branch of continuum mechanics; solid and fluid mechanics. The aspect here will be on solid, specifically rock mechanics, and a small part on fluid flow within the rock. First, an introduction to fluid flow in porous media will be explained before some general principles of rock mechanics will be given. Afterwards the more specific task of understanding the impact thermal, hydraulic and mechanical stresses have on the deformation of fractured porous media will be explored.

The mass and energy conservation, and the force/stress balance are the most important governing equations, and are absolutely necessary to be able to describe THM processes in fractured porous media. The equation of motion for a porous media is used to describe the stress balance, and to describe heat and fluid flow, Fourier's and Darcy's law are used respectively.

3.1 Governing Equations

3.1.1 Darcy's law

Darcy's law governs flow in porous media and gives a relationship between the flow of the fluid and the pressure. Darcy's law is an empirical relationship which was found from measuring the flow between two points in a cylindrical sand column. Darcy observed that the volumetric flow rate per area q was proportional to the the difference between the hydraulic heads h and inversely proportional to the distance L between the measurement points.

$$q = -k\frac{(h_2 - h_1)}{L} \tag{1}$$

where k is the proportionality constant called the hydraulic conductivity. Generalizing to a multi-dimensional case and taking the limit as L goes to zero will result in

$$\vec{q} = -k\nabla h. \tag{2}$$

The hydraulic head can be defined as [Nordbotten and Celia2012]:

$$h = \frac{p}{\rho_f g} + z \tag{3}$$

Substituting for h with eq. (3) and assuming incompressibility results in Darcy's equation for single-phase flow [Nordbotten and Celia2012]:

$$\vec{q} = -k\nabla(\frac{p}{\rho_f g} + z) = -\boldsymbol{k}(\nabla p + \rho g \nabla z), \tag{4}$$

where $\boldsymbol{k} = \frac{k}{\rho g}$

3.1.2 Fluid mass conservation

Since the pressure is unknown the flow through a porous medium cannot be described by Darcy's law alone, and another equation is therefore needed. This additional equation comes from mass conservation. The idea is to look at a region of space and make the observation that the change in mass of a substance in that region must be equal to the inflow and outflow of mass through the boundary, plus any mass that appears or disappears within the region without passing through the boundary. This can be stated mathematically as

$$\int_\Omega \frac{\partial m_f}{\partial t}\, dV = -\int_{\partial\Omega} \rho_f \vec{q} \cdot \vec{n}\, dA + \int_\Omega \psi\, dV, \tag{5}$$

Where m_f is representing the mass per total volume of porous medium, $\vec{q}$ is the flow vector, t is time and ψ is a source or sink term of mass within the volume. These variables can be defined as

$$m_f = \rho_f \phi \tag{6}$$

where ϕ is the porosity defined as the ratio between the volume of the pores, V_P, and the total volume V_T, i.e volume of the pores plus the solid part. $\phi = \frac{V_P}{V_T}$ and $\vec{q}$ is the flux vector.

Inserting (6) into (5) and applying the divergence theorem results in the equation

$$\int_\Omega \frac{\partial(\rho_f \phi)}{\partial t}\, dV = -\int_\Omega \nabla \cdot (\rho_f \vec{q})\, dV + \int_\Omega \psi\, dV. \tag{7}$$

By moving the first term on the right hand-side to the left hand-side and observing that the integral in (7) has to hold for an arbitrary closed volume Ω, it must be the case that the integrand itself is zero, which will result in the general mass conservation equation for a single phase fluid.

$$\frac{\partial(\rho_f \phi)}{\partial t} + \nabla \cdot (\rho_f \vec{q}) = \psi. \tag{8}$$

3.1.3 Conservation of linear momentum for a solid

Another important set of equations in rock mechanics are the equations of motion, alternatively stated as the equations of stress equilibrium if the rock is in static equilibrium. These equations can be derived by applying the law of conservation of linear momentum to the rock, known as Newton's second law if the mass is conserved. Newton's second law states that the total force applied to a body in a given direction will be equal to the mass of the body multiplied by its acceleration $\vec{a}$ in that direction

$$\vec{F} = m\vec{a}. \tag{9}$$

The total forces which are applied to a rock will be the body forces $\vec{b}$ due to gravity acting over the internal portions of the rock, plus the tractions $\vec{T}$ acting along the surface of the rock [Jaeger et al.2007]. The acceleration will be given by the second partial derivative of the displacement $\vec{u}$, with respect to time. Newton's second law can then be written as

$$\int_{\partial\Omega} \vec{T}\ dA + \int_{\Omega} \vec{b}\ dV = \int_{\Omega} \rho \frac{\partial^2}{\partial t^2}\vec{u}\ dV. \tag{10}$$

Expressing the traction vector in terms of the stress tensor

$$\vec{T} = \boldsymbol{\sigma} \cdot \vec{n}, \tag{11}$$

where $\vec{n}$ is the normal vector. Inserting eq. (11) into eq. (10) produces the expression

$$\int_{\partial\Omega} \boldsymbol{\sigma} \cdot \vec{n}\ dA + \int_{\Omega} \rho\vec{b}\ dV = \int_{\Omega} \rho \frac{\partial^2}{\partial t^2}\vec{u}\ dV. \tag{12}$$

Applying the divergence theorem to the first term on the left hand side results in the equation

$$\int_{\Omega} (\nabla \cdot \boldsymbol{\sigma} + \rho\vec{b})\ dV = \int_{\Omega} \rho \frac{\partial^2}{\partial t^2}\vec{u}\ dV. \tag{13}$$

Using the same argument as in the derivation of the mass conservation equation, the integrand must be zero, because the equation must hold for any arbitrary sub region of the rock mass. The equation of motion follows:

$$\nabla \cdot \boldsymbol{\sigma} + \rho\vec{b} = \rho \frac{\partial^2}{\partial t^2}\vec{u} \tag{14}$$

In order to solve a problem for an isotropic rock (rock with identical values of certain properties in all directions) it is important to ensure that the problem actually has a solution, that it is well posed. The equations of motion for a deformable body defined earlier as eq. (14) are needed to ensure the well posedness, which applies to all deformable bodies, and has to be satisfied regardless of the particular stress-strain relationship.
The rock is assumed to be in static equilibrium or the displacements will occur very slowly, meaning that the change in displacement will be set to zero. The equation of motion can then be better named the equation of stress equilibrium and expressed as

$$\nabla \cdot \boldsymbol{\sigma} + \rho\vec{b} = 0 \tag{15}$$

The stress equilibrium equations are very general in the sense that no assumptions on the stress-strain behavior of the rock is made. If the assumption that the rock is made of a linearly elastic material is made, the equation can be expressed in terms of the displacements.

3.1.4 Energy

So far the governing equation for solving a mechanics problem has been derived. However, in order to understand how thermoelasticity plays a role in the behaviour of thermally dependent parameters, some understanding of energy is needed.
Conservation of energy, states that the energy of an isolated system remains constant, which means that energy cannot be created or destroyed, only change in form. An isolated system means that neither energy nor mass outside the boundary of the system can pass through.

The first law of thermodynamics, is a form of the conservation of energy, and states that the change in internal energy of a closed system is due to heat transferred to the system and work done by the surroundings on the system. Where closed in this sense is defined as energy being able to pass through the boundary, but not matter. The first law of thermodynamics, can be stated as follows:

$$\frac{D}{Dt}E = \frac{D}{Dt}Q + \frac{D}{Dt}W^{def}, \tag{16}$$

where $E = U + K$ is the total energy of the system, U is the internal energy, K is the kinetic energy, Q is the heat transferred to the system and W is the work happening to the system. The kinetic energy can be defined as follows:

$$K = \int_\Omega \frac{1}{2}\rho\vec{v}\cdot\vec{v}\ dV, \tag{17}$$

$\frac{D}{Dt}$ denotes the material derivative and is defined as

$$\frac{D}{Dt}(.) = \frac{\partial}{\partial t}(.) + \frac{\partial}{\partial x}(.)\frac{dx}{dt}. \tag{18}$$

it is used whenever considering time rate of change where the properties of the material itself depends on time.

The internal energy can be expressed as

$$U = \int_\Omega \rho u\ dV, \tag{19}$$

where the change in the internal energy can be expressed as

$$\frac{D}{Dt}U = \frac{D}{Dt}\int_\Omega \rho u\ dV = \int_\Omega \rho\frac{D}{Dt}u\ dV. \tag{20}$$

Moreover, the heat transfer rate can be divided into a heat source within the domain and a heat flux going through the boundary

$$\frac{D}{Dt}Q = \int_\Omega \rho r\ dV - \int_{\partial\Omega}\vec{c}\cdot\vec{n}\ dA, \tag{21}$$

where $r = r(x,t)$ is an external source of energy per unit mass and $\vec{c}$ is the heat flux vector.

To derive the work of deformation happening inside the domain, it is useful to look at the total external work being done to the domain. The external work being done will be due to body and traction forces

$$W = \int_\Omega \rho\vec{b} \cdot \vec{v} \ dV + \int_{\partial\Omega} \vec{T} \cdot \vec{v} \ dA, \tag{22}$$

$\vec{v}$ is the velocity and $\vec{T}$ is the surface traction and can be expressed with the stress tensor as $\vec{T} = \boldsymbol{\sigma} \cdot \vec{n}$

Applying this relationship, and the divergence theorem to the second term on the right hand side of eq. (22) yields

$$\int_{\partial\Omega} (\boldsymbol{\sigma}\vec{v}) \cdot \vec{n} \ dA = \int_\Omega \nabla \cdot (\boldsymbol{\sigma}\vec{v}) \ dV = \int_\Omega (\nabla \cdot \boldsymbol{\sigma}) \cdot \vec{v} + \boldsymbol{\sigma} : \nabla\vec{v} \ dV, \tag{23}$$

where : is defined as the double dot product between two tensors.

Inserting eq. (23) into eq. (22) results in

$$\frac{D}{Dt}W = \int_\Omega (\rho\vec{b} + \nabla \cdot \boldsymbol{\sigma}) \cdot \vec{v} \ dV + \int_\Omega \boldsymbol{\sigma} : \nabla\vec{v} \ dV \tag{24}$$

By observing that the first term on the right hand side of eq. (24) is the equation of motion eq. (15)

$$\rho\vec{b} + \nabla \cdot \boldsymbol{\sigma} = \rho\vec{a}, \tag{25}$$

where $\vec{a}$ is the acceleration vector being defined as the material derivative of the velocity vector.

and therefore substituting eq. (25) into eq. (24) yields the equation

$$\frac{D}{Dt}W = \int_\Omega \rho\vec{a} \cdot \vec{v} + \boldsymbol{\sigma} : \nabla\vec{v} \ dV \tag{26}$$

Now the first term on the right hand side of eq. (26) is actually the change in the kinetic energy as it can be expressed as

$$\frac{D}{Dt}K = \frac{D}{Dt}\int_\Omega \frac{1}{2}\rho\vec{v} \cdot \vec{v} \ dV = \int_\Omega \rho\vec{a} \cdot \vec{v} \ dV. \tag{27}$$

Using this fact eq. (26) becomes

$$\frac{D}{Dt}W = \frac{D}{Dt}K + \frac{D}{Dt}W^{def}, \tag{28}$$

where W^{def} is the work due to deformation

$$\frac{D}{Dt}W^{def} = \int_{\Omega} \boldsymbol{\sigma} : \nabla \vec{v} \; dV. \tag{29}$$

Finally eq. (29), (20) and (21) can be substituted into the first law of thermodynamics eq. (16) to get the following equation

$$\int_{\Omega} \rho \frac{Du}{Dt} - \boldsymbol{\sigma} : \nabla \vec{v} - \rho r \; dV = - \int_{\partial\Omega} \vec{q} \cdot \vec{n} \; dA. \tag{30}$$

It can be thought of as the conservation of internal energy for an infinitesimal continuum particle where $\boldsymbol{\sigma} : \nabla \vec{v}$ is the rate of change in the mechanical work (power) going towards the deformation of the particle; ρr is the internal source of heat and $\vec{q}$ is the inflow of heat through the boundaries of the particle [Tadmor et al.2011].

If the rate of change in the mechanical work of deformation and the internal heat source are neglected, the standard diffusion equation for the temperature will follow. That is the change in the heat dependent part of the internal energy inside the rock must be equal to the heat flux coming through the boundary of the rock

$$\int_{\Omega} \rho \frac{D}{Dt} u \; dV = - \int_{\partial\Omega} \vec{c} \cdot \vec{n} \; dA. \tag{31}$$

Using the divergence theorem on eq. (31), and knowing that eq. (31) is satisfied for an arbitrary body results in the following equation

$$\rho \frac{D}{Dt} u = -\nabla \cdot \vec{c}. \tag{32}$$

Here u can be written as $u = u_o + C_v T$ where u_o is some arbitrary reference energy and C_v is the specific heat at constant strain. By Fourier's law the heat flux vector can be written as

$$\vec{c} = -\boldsymbol{h} \nabla T, \tag{33}$$

where $\boldsymbol{h}$ is a thermal conductivity tensor. Putting these terms into eq. (32) will result in a diffusion equation which governs heat conduction through a rigid medium

$$\rho \frac{D}{Dt}(u_o + c_v T) = -\nabla \cdot (-\boldsymbol{h} \nabla T) \tag{34}$$

$$\Rightarrow \frac{D}{Dt} T = \frac{\boldsymbol{h}}{\rho C_v} \nabla^2 T. \tag{35}$$

3.2 Constitutive models

3.2.1 Linear elasticity

When a strong enough force is applied to a solid body, a deformation occurs. Elasticity is the ability of the solid body to return to its original shape or form after the force is removed. All materials have different elastic properties, which are defined in term of its elastic moduli. There are different types such as Young's E, bulk K and shear modulus G. The problem of elasticity is to determine the stresses and displacements of a body that occur due to prescribed displacements or tractions along its outer boundary, and prescribed forces at its interior points.

Linear elasticity is a relationship between stress and strain in which the strain tensor $\mathcal{E}$ is a linear function of the stress tensor $\boldsymbol{\sigma}$. No rocks are linearly elastic over a wide range of stresses, however, it is still quite a useful approximation since most rocks behave linearly for incremental changes in stress.
The governing equation needs to be supplemented by a set of constitutive equations, which describes the relationship between stress, strain and possibly other parameters such as temperature, pore pressure etc. In the case of this thesis the temperature will be an important factor. In order to ensure a unique solution, where linear elastic behavior is assumed, boundary conditions and restrictions on the value of the elastic moduli are also needed.

For the constitutive equations, the general stress-strain relationship, assuming infinitesimal strain is given by

$$\boldsymbol{\sigma} = \mathbb{C} : \mathcal{E}. \tag{36}$$

Where $\mathbb{C}$ is a 4th order stiffness tensor and the strain tensor $\mathcal{E}$ is given by the strain-displacement (compatibility) equations:

$$\mathcal{E} = \frac{1}{2}[\nabla\vec{u} + (\nabla\vec{u})^T], \tag{37}$$

where $\vec{u}$ is the displacement vector.
Now assuming that the rock is isotropic, a linear relationship between the stress and strain is obtained with the use of Hooke's law.

$$\boldsymbol{\sigma} = 2G\mathcal{E} + \lambda trace(\mathcal{E})I, \tag{38}$$

where λ is the elastic modulus (Lamé's first parameter), G is the shear modulus (Lamé's second parameter), I is the identity tensor

A combination of the governing, constitutive and compatibility equations give the Navier-Cauchy equations, that is, inserting eq. (37) into eq. (38) and then inserting this into eq. (15) yields

$$(\lambda + G)\nabla(\nabla \cdot \vec{u}) + G\nabla^2\vec{u} + \rho\vec{b} = 0. \tag{39}$$

They embody the equations of stress equilibrium, stress-strain equations and strain-displacement equations. The strain displacement equations are used in Hook's law to eliminate the strains as unknowns, Hooke's law is then substituted in the equation of stress equilibrium to get the Navier-Cauchy equations. The remaining unknown functions will then be the displacements, hence in order to be able to find the displacements there has to be Dirichlet boundary conditions, which specifies the displacement on the boundary of the domain, or additionally Neumann boundary conditions, which specifies the traction on the boundary.

For the Navier equations there are as many equations as there are unknowns, that is 3 equations for 3 unknowns, which is a necessary requirement for a given elasticity problem to be solvable. However, in general there will be an infinite number of functions, which satisfy the equations. So in order to find the actual displacements some knowledge of the displacements along the outer boundary of the rock mass is needed. This is given by the uniqueness theorem of linear elasticity, which roughly states that if the traction or displacements are known at each point of the outer boundary, then a unique solution to the governing elasticity problem exists. The practical importance of this theorem is that the conditions of the theorem specify the amount of information that is needed about the boundary in order to be able to solve the elasticity equations [Jaeger et al.2007].

3.2.2 Elastic moduli

Elastic moduli are parameters which describe the relationship between stress and strain in elastic materials. The general relationship is defined as

$$\mathbb{Y} = \frac{\boldsymbol{\sigma}}{\mathcal{E}}. \tag{40}$$

It is an objects or materials resistance to elastic deformation by an applied stress. Since stress and strain can be applied in different directions and measured in several ways there are different kinds of Elastic moduli.

One of them is Poisson's ratio $\mathcal{V}$ which is the ratio between transverse strain to longitudinal axial strain in the direction of stretching force:

$$\mathcal{V} = \frac{\mathcal{E}_{trans}}{\mathcal{E}_{axial}}. \tag{41}$$

This phenomena is for instance seen when stretching a material and the material contracts in the direction transverse to the stretching.

Another important elastic moduli is Young's modulus E, which is the ratio between tensile or compressive stress and strain:

$$E = \frac{\boldsymbol{\sigma}_n}{\mathcal{E}}. \tag{42}$$

It is the tendency of an object to deform along the axis in which the stress is being applied. It is an intrinsic property of the material. However, it is dependent on temperature, since changes to the temperature may affect the fundamental structure of the material.

Young's modulus E can be divided into static and dynamic Young's modulus E_s and E_d respectively. E_s reflects the mechanical properties of rocks and are calculated by using mechanical tests while E_d reflects the physical properties of rocks and are calculated from elastic average velocity and density tests. The relationship between E_s and E_d is quite complex, but it is found that the dynamic Young's modulus decreases faster with temperature than for the static case Liu [Liu and Xu2015].

Lame's parameters are also very important since they are used in defining the stiffness tensor $\mathbb{C}$. The first lame parameter λ can be expressed as

$$\lambda = \frac{E\mathcal{V}}{(1+\mathcal{V})(1-2\mathcal{V}}, \tag{43}$$

and the second one, also named the shear modulus G, as

$$G = \frac{E}{2(1+\mathcal{V})}. \tag{44}$$

3.3 Fracture Mechanics

A fracture in a rock is a separation of the rock into two or more parts. For an idealized fracture, there will be two parts, consisting of two planar rough surfaces. The surfaces will usually touch each other at certain points, but will be separated at other points. The distance of separation in the fracture is called the aperture and will usually be measured perpendicular to the fracture plane.

To describe a fracture in 2-D one can think of a planar fracture that lies in the x-y plane, where two parallel reference planes are defined: one inside the upper region, and one inside the lower region of the rock respectively.

The length between the bottom reference plane and the lower fracture surface can then be defined as a height function $h_1(x, y)$ and likewise for the upper fracture surface as $h_2(x, y)$. The distance between the reference planes is defined as d and the aperture can then be defined as

$$L(x, y) = d - h_2(x, y) - h_1(x, y) \tag{45}$$

The idea is illustrated in the following figure

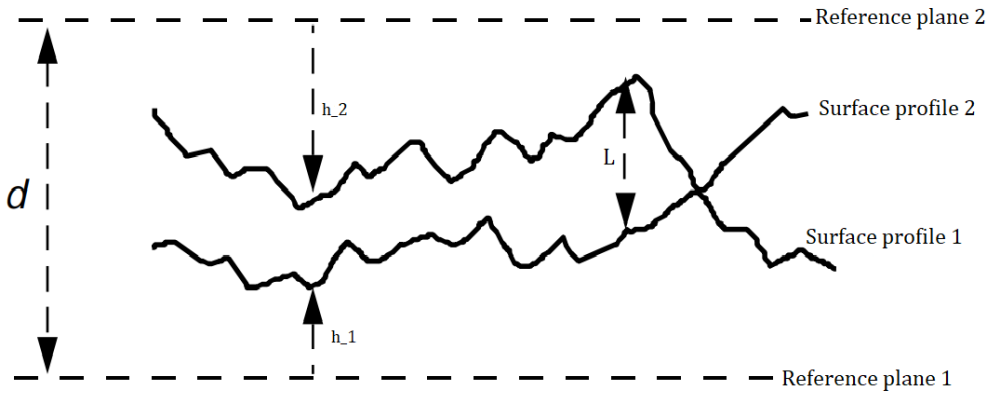

Figure 1: Illustration of a fracture from [Jaeger et al.2007]

The aperture will fluctuate since it is a measure between rough, not smooth surfaces. In general a fracture is said to be open if the aperture is greater than 10mm, and closed if its smaller than 0.25mm. An open fracture usually contains air, water or other fluids while a closed fracture is filled by fault rock or other injected materials.

3.4 Friction law

Friction is the force that resists the motion between surfaces, and can be described by the following example.

Imagine we have a box on top of a planar surface pressed together by a normal traction force T_n. If a shearing traction force T_s is applied to the side of the box parallel to the plane of contact, it will eventually start moving after the force has reached a critical value.

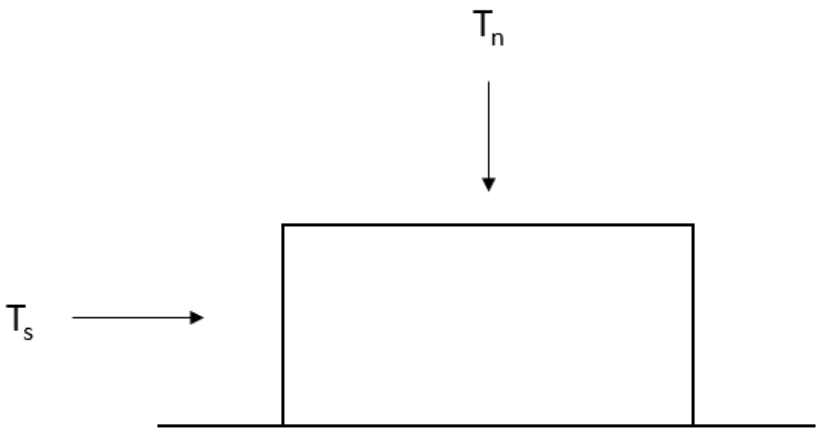

Figure 2: Illustration of the force of friction based on Amonton's law

This relationship between the normal and shear stress is Amonton's law, and can be described as

$$T_s = \mu T_n, \tag{46}$$

where μ is the coefficient of friction. The coefficient of friction is dependent on the nature of the surfaces and in some cases on the normal stress. If there is movement between the surfaces the coefficient is called the kinetic friction coefficient μ_k and if the surfaces are stationary it is called the static friction coefficient μ_s. Where $\mu_k \leq \mu_s$ that is, ones sliding has been initiated it requires less shear stress to maintain motion than it required to initiate it. The coefficient of friction is a non-dimensional unit i.e a scalar varying mostly in the range from 0 to 1. However, it can be much greater than 1. Where 0 represents that there is no friction between the surfaces and 1 means that the frictional force is equal to the normal stress.

3.4.1 Coulomb's law

The frictional effects are somewhat different for rocks as the coefficient of friction will be different due to a change of surface. It is found that the coefficient of friction will increase with increasing normal stresses, but stabilize at high enough normal traction value T_n. However, when the shear traction T_s is plotted against the normal traction T_n the data falls on a nearly straight line. A better description for rock friction specifically is then Coulomb's law:

$$T_s = S_o + \mu T_n, \tag{47}$$

where S_o is the cohesion. What this simply means is that if there were no normal tractions T_n there would still be a need of a shear force equal or greater than the cohesion force S_o.

A criterion for slip to occur is therefore that

$$|T_s| \geq \mu |T_n| + S_o \tag{48}$$

It is interesting to see how the law can be applied to a plane of weakness, specifically the sliding/reactivation of fractures in this thesis.

Imagine there is a rock which has a preexisting fracture of weakness whose outward unit normal vector $\vec{n}$ makes an angle α to the direction of the maximum principal stress σ_{11}

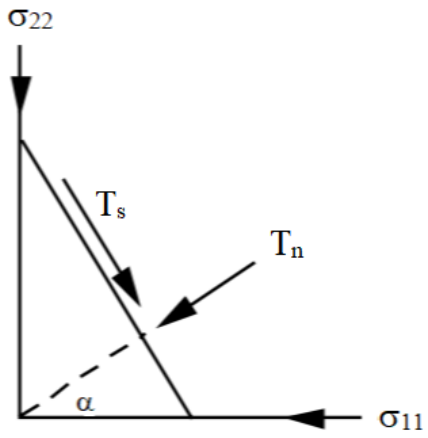

Figure 3: Plane of weakness, figure adapted from [Jaeger et al.2007]

where $\sigma_{11} > \sigma_{22}$ are the principal stresses. The condition for where slip will occur according to Coulomb's law can be represented visually with the Mohr diagram which is derived in [Jaeger et al.2007].

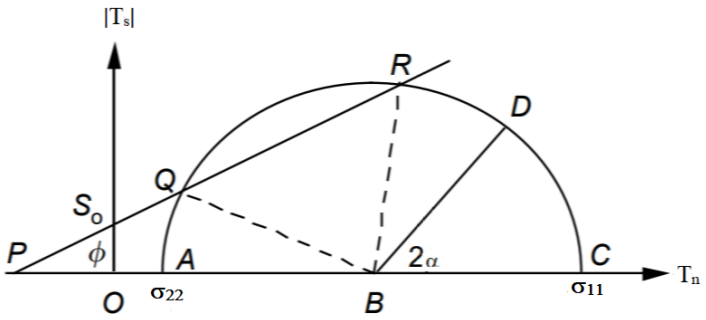

Figure 4: Mohr Diagram, figure adapted from [Jaeger et al.2007]

The condition for slip (eq. 48) is visualized as the line PQR in Fig. 4 which is oriented at an angle of α to the normal traction T_n and intercepts the $|T_s|$ axis at S_o. The normal and shear tractions along the plane of weakness is illustrated by the point D. Slip will only occur if the point D is inside the arc Q-R

3.4.2 Slip tendency

A useful tool for making predictions of where displacement will occur on a fracture is a measure of the slip tendency. The slip tendency is a measure of a fault surface's tendency

to slip and depends on stress and the coefficient of friction. It is based on Coulomb's law (eq. 48), but it is assumed that the fracture has no cohesion.

If $|T_s| < |T_n|$ no slip will occur. However, as soon as

$$|T_s| \geq \mu |T_n| \tag{49}$$

slip will occur. The slip tendency is calculated as the ratio between the absolute value of the shear and normal stress as follows

$$ST = \frac{|T_s|}{|T_n|} \tag{50}$$

where ST is defined here as the slip tendency.

3.5 Constitutive temperature dependent relationships

3.5.1 Temperature effects on Young's modulus

The relationship between temperature T and Young's modulus E is quite complicated, but it has been shown that Young's modulus of rocks decrease linearly with temperature as the temperature increases [Sygała et al.2013]. However, major changes to Young's modulus won't happen until the temperature has reached a critical point.

Liu [Liu and Xu2015] did an simulational study for temperature effects on static Young's modulus for granite and found the following values for different temperatures.

Temperature C°	Static Young's modulus GPa
20	39.30
100	34.92
200	29.22
400	18.97

Figure 5: Table with values of temperature and Young's modulus for granite [Sygała et al.2013].

An exact linear relationship from $50 - 500$℃ has been based of these values, which is not far from the actual values found. The slope has been calculated from taking the difference in temperature

$$400 - 20℃ = 380℃ \tag{51}$$

and the difference in Young's modulus

$$39.30 - 18.97 = 20.33GPa \implies 1℃ = \frac{3}{56}GPa. \tag{52}$$

Therefore E at 50℃ will be E at

$$20℃ - \frac{3}{56}GPa \times 30 = 37.7GPa. \tag{53}$$

Likewise E at 500℃ will be E at

$$400℃ - 100 \times \frac{3}{56}GPa = 13.61 \tag{54}$$

The relationship is illustrated in the following figure

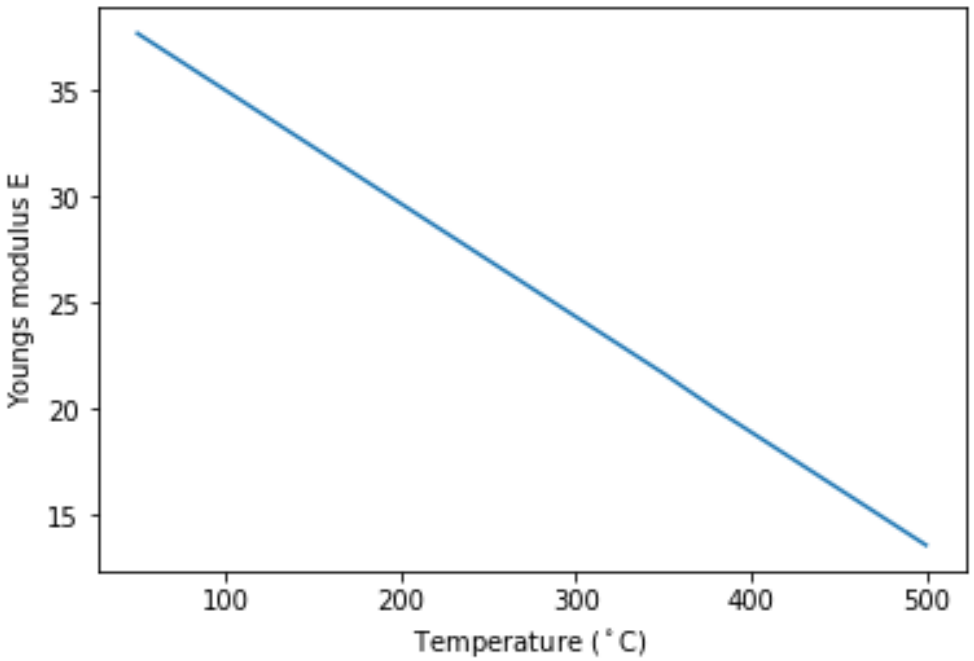

Figure 6: Young's modulus vs temperature

The effects that temperature has on the mechanical properties of rocks has been observed in several simulations [Zhang et al.2009], [Tian et al.2017] and is done by first heating the rock samples to the desired temperature before cooling them down. However, this is not sufficient to reflect the essential characteristics of rocks at high temperatures, as heating a rock causes irreversible thermal expansion, and cooling the rock thereafter causes changes in the micro-structure of the rock.
[Zhang et al.2009] looked at marble, limestone, and sandstone as the temperatures varied from 20-1000℃ and found that all rock types have Young's modulus E gradually decrease in the range of $200 - 400$℃ although there were some variations between rock types, and Young's modulus drops faster after this. After 600℃ it is safe to say that all rocks experience a drastic drop in Young's modulus. To illustrate just how much Young's modulus

actually decreases at really high temperatures [Tian et al.2017] showed that Young's modulus decreased by 82% at 800℃ and 93% at 1000℃ for diorite rocks compared to that of room temperature.

The reason for this drastic drop in Young's modulus is because of the change in rock structure. As the temperature increases variations in the thermal expansions of the minerals within the rock, causes thermal stress, which in the temperature range of $400 - 600$℃ exceeds the maximum strength of the rock, resulting in the creation of new micro-cracks. This will damage the rock structure, which means more strain, and therefore a reduction in Young's modulus [Sygała et al.2013].

Whether a uniaxial compression test or a propagation velocity test is used, it does n0t influence the results much according to [Brotons et al.2013]. This study showed a 75% and 78% reduction in Young's modulus from $105 - 600$℃ for air and water cooled samples respectively. The study also showed a 40% and 68% reduction for Poisson's ratio for air and water cooled samples. Where both the regular mechanical test and the ultrasonic propagation velocity test was used with very similar results for both elastic moduli.

It is important to keep in mind that this study cooled the samples after heating. So as noted earlier, the results will not be fully accurate. However, it still goes to show the general trend of decrease in Young's modulus and poison's ratio as the temperature increases.

3.5.2 Temperature effects on friction

As the domain where the slip tendency will be calculated involves a temperature gradient it is important to know if the coefficient of friction depends on temperature. This is because the value of the slip tendency will change based on the value of the friction coefficient. The coefficient of friction μ has been shown to depend on temperature, and is also dependent on the material in question, and whether the kinetic μ_k or static μ_s coefficient of friction is desired [Pouzada et al.2006].

In general, it is much more difficult to measure the relationship between frictional behaviour and temperature in rocks due to factors outside of temperature playing a role. For instance, roughness of the surfaces, fluid pressures, gauge forming between the surfaces etc. When sliding occurs between surfaces the coefficient of friction will eventually go toward a steady state value μ_v^{ss} for any sliding rate V.

The change in the steady state when the velocity changes from V to V^* can be described as

$$\Delta\mu_{ss} = Bln(V^*/V) \tag{55}$$

where B is the rate dependence of frictional sliding strength, but may slightly depend on

the velocity as it is still not well characterized and continuous to elude detailed understanding.

Furthermore, this is only a theoretical coefficient, since in practice there has never been observed that a fault approaches a time-invariant shear strength if it is deformed at constant normal stress and velocity [Lockner et al.1986].

There have been several studies on the coefficient B. For instance from studies using a triaxial shear test, it is been found that there is not a huge correlation between B and temperature variations. A test result from [Stesky1975] showed that B increased from 0.003 at 300℃ to 0.021 at 700℃. However, [Lockner et al.1986] looked at four studies, including its own and the study of Stesky and showed that there were no correlation between temperature and B and concluded that it was caused by other factors such as removal of adsorbed water, different test geometries etc.
The role of temperature dependence on friction for rocks is quite complicated and is hard to find because of several factors. In some cases the friction strength increases as the temperature increases due to removal of adsorbed water or the formation of glass. However, in other scenarios the friction strength is unaffected or decreases as the temperature increases most likely due to weakening of the material on the fault surface [Stesky1978]. In other scenarios varying test techniques are used or the coefficient is dependent on other unknown factors. There is also the important case that once two surfaces move on top of each other, gauge will immediately be produced, forming a third layer between the two surfaces. These considerations make the study of the friction coefficient between two surfaces more of an idealization than reality. Due to these considerations the coefficient of friction will be set to a constant value for the problem in this thesis.

3.6 Model problem

The general problem at hand can now be discussed before delving into the numerical methods. The equation of stress equilibrium with no body forces will be solved.

$$\begin{aligned} \nabla \cdot \boldsymbol{\sigma}_{bc} &= 0 \ \ in \ \ \Omega \\ \vec{u}_{|\partial\Omega_d} &= \vec{u}_d \\ (\boldsymbol{\sigma}_{bc} \cdot \vec{n})_{|\partial\Omega_n} &= \vec{t}_n, \end{aligned} \tag{56}$$

where $\boldsymbol{\sigma}_{bc}$ is the stress due to the boundary conditions, u_d are the Dirichlet displacement boundary conditions, $\vec{t}_n$ are the Neumann traction boundary conditions. The flow problem will also be solved:

$$
\begin{aligned}
\nabla \cdot \vec{q} &= 0 \\
\vec{q} &= -\boldsymbol{k}\nabla p \\
-\nabla \cdot \boldsymbol{k}\nabla p &= 0 \\
p_{|\partial\Omega_d} &= p_d \\
\vec{q}_{|\partial\Omega_n} &= \vec{q}_n,
\end{aligned}
\tag{57}
$$

where p_d are the Dirichlet pressure boundary conditions and $\vec{q}_n$ are the Neumann flow boundary conditions.

It should be noted that the stress will be a combination of the background stress and the internal stress due to the boundary conditions.

$$
\boldsymbol{\sigma} = \boldsymbol{\sigma}_{bs} + \boldsymbol{\sigma}_{bc} \tag{58}
$$

The principle of superposition will therefore briefly be explained. The principle states that for all linear systems the net response caused by two or more stimuli will be the same as the sum of each stimulus done individually. A function $G(x)$ that satisfies the superposition principle is called a linear function. The principle can be derived by the property of additivity and homogeneity

$$
\begin{aligned}
G(x_1 + x_2) &= G(x_1) + G(x_2) \quad \textit{Additivity} \\
G(cx_1) &= cG(x_1), c \in \mathbb{R} \quad \textit{homogeneity}
\end{aligned}
\tag{59}
$$

4 Numerical model

The multi-point stress approximation (MPSA) method will be used to solve the mechanical problem at hand, while the multi-point flux approximation (MPFA) method will be used to solve the flow problem. Both of these methods will be covered later in the chapter. However, first a few methods which the methods are based on will be covered.

4.1 Finite volume method

In order to simulate and produce results for the simulations that will be done later on, an understanding of the numerical methods that are used will be needed. The fundamental numerical method used in this thesis which all the other methods are built upon is the finite volume method. The finite volume method (FVM) is a numerical method used to solve partial differential equations (PDE's), especially those that arise from physical conservation laws.

FVM is an integral formulation of the problem with a finite partitioning set of volumes to discretize the equations. The continuous domain where the PDE is defined on gets partitioned into a domain of smaller meshes, called the finite cells. The PDE is then represented by its values on certain points of the mesh. In other words the PDE is replaced by a linear system of algebraic equations. There are two types of FV methods, the cell vertex and the cell centered. The latter one is used in this thesis. As an example, the poisson's equation in 2-D is used.

$$\Delta u = f \ \ in \ \ \Omega, \tag{60}$$

which can be rewritten in divergence form as

$$\nabla \cdot \nabla u = f \ \ in \ \ \Omega. \tag{61}$$

The idea now is to integrate over small volume elements of Ω called finite volumes.

$$\int_{\Omega} \nabla \cdot \nabla u \ \ d\Omega = \int_{\Omega} f \ \ d\Omega, \tag{62}$$

by using the divergence theorem the equation becomes

$$\int_{\partial\Omega} \nabla u \cdot \vec{n} \ \ dS = \int_{\Omega} f \ \ d\Omega. \tag{63}$$

So the equation says that the sum of the flux that comes in and out of our control volume must be equal to the source term f. This idea is why the FV is used for conservation problems.
A mesh is generated out of the domain Ω and its boundary $\partial\Omega$ which can be defined as follows

$$\Omega = \bigsqcup_{i=1}^{m} \Omega_i \ \ and \ \ \partial\Omega_i = \bigsqcup_{j=1}^{n} \Gamma_{ij} \tag{64}$$

where Γ_{ij} are the edges between each node of the domain boundary.

By integrating over Ω_i it follows that

$$\int_{\partial\Omega_i} \nabla u \cdot \vec{n} \ \ dS = \int_{\Omega_i} f \ \ d\Omega \tag{65}$$

replacing Ω_i with Γ_{ij} yields

$$\sum_{j=1}^{N} \int_{\Gamma_{ij}} \nabla u \cdot \vec{n}_{ij} \ \ dS = \int_{\Omega_i} f \ \ dA, \tag{66}$$

where N are the number of edges.

The idea is then that the global problem is solved by splitting the problem into several smaller local problems, followed by solving these problems and combining their solutions to get the global solution. The source term f is assumed to be constant, so it will be trivial to approximate. However, what is not trivial, is how to approximate the flux term ∇u which will be discussed in the following two sections. The next two methods are inspired by the book "Elliptisk" by [Aavatsmark2007].

4.2 Two-point-flux-approximation method (TPFA)

The general conservation problem for a cell is

$$\int_{\partial\Omega_i} \vec{q} \cdot \vec{n} \ \ dS = -\int_{\Omega_i} f \ \ dV \tag{67}$$

where $\vec{q}$ is the flux vector and f is the source term.
The two-point-flux approximation method, as the name implies, is used to find an approximation to the flux across each edge of the cell

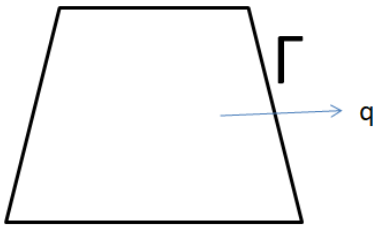

Figure 7: Flux through an edge Γ

where the flux over an edge Γ can be described by the flux density equation

$$\vec{q} = -\int_{\Gamma} K\nabla p \cdot \vec{n}\ dS = -\int_{\Gamma} \nabla p \cdot \vec{w}\ dS \tag{68}$$

Where K is a positive definite permeability tensor assumed to be constant in each cell, $\vec{w} = K \cdot \vec{n}$ and p is a potential.
The idea of the method is that the flux over an edge can be approximated by using known values of u in two adjacent cells sharing the same edge. Since K is positive definite $n^T K n > 0$ which means that $\vec{w}$ will point in the same direction as $\vec{n}$. However, $\vec{w}$ can have different directions on each cell, since K can vary from cell to cell. Due to this fact, the values of p in the points x used to approximate the flux $\vec{q}$ has to be in the same direction as $\vec{w}$
Fig. (8) is a good illustration of the point

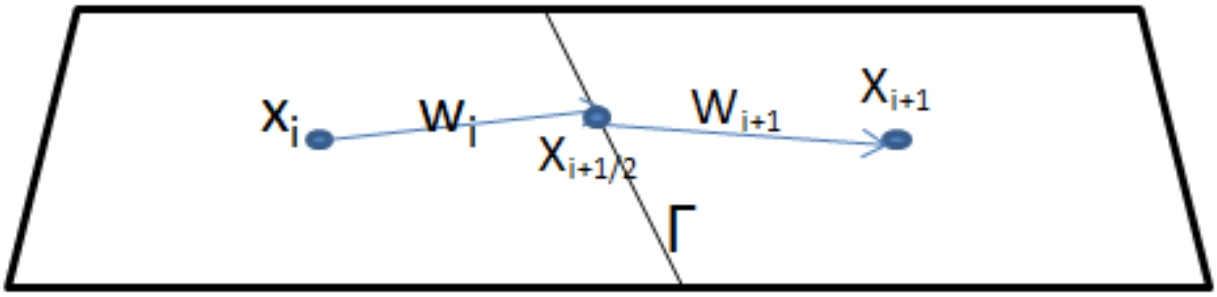

Figure 8: Two-point-flux-method, figure adapted from [Aavatsmark2007]

By using the definition of $\vec{q}$, looking at Fig. (8) and recalling that $\nabla\vec{u}$ can be approximated as

$$\nabla\vec{u} \approx \frac{u(x_{i+1}) - u(x_i)}{h} \tag{69}$$

the flux can be approximated for the first cell as

$$q = \Gamma \frac{u(x_{i+1/2}) - u(x_i)}{||x_{i+1/2} - x_i||_2} \cdot \vec{w}_i \implies u_{i+\frac{1}{2}} - u_i = \frac{q}{\Gamma} \frac{||x_{i+1/2} - x_i||_2}{||K_i n||_2} \tag{70}$$

The flux for the second cell can be approximated in the same way, which results in

$$q = \Gamma \frac{u(x_{i+1}) - u(x_{i+\frac{1}{2}})}{||x_{i+1} - x_{i+\frac{1}{2}}||_2} \cdot \vec{w}_{i+1} \implies u_{i+1} - u_{i+\frac{1}{2}} = \frac{q}{\Gamma} \frac{||x_{i+\frac{1}{2}} - x_i||_2}{||K_{i+1} n||_2} \tag{71}$$

The value $u(x_{i+\frac{1}{2}})$ is not known, however since the flux is continuous over the cell wall, the value in $u(x_{i+\frac{1}{2}})$ has to be the same on each side of the cell wall. So eq. (70) can be

substituted inside eq. (71) arriving at the following equation for the flux across the cell wall

$$q_{i+\frac{1}{2}} = \Gamma(u_{i+1} - u_i)(\frac{||K_{i+1}\vec{n}||_2}{||x_{i+1} - x_{i+\frac{1}{2}}||_2} + \frac{||K_i n||_2}{||x_{i+\frac{1}{2}} - x_i||_2}) \tag{72}$$

These approximations can only be made if the connection between the points $\vec{x}$ are parallel to the direction of $\vec{w}$. That is, the line connecting $\vec{x}_i$ and $\vec{x}_{i+\frac{1}{2}}$ has to be parallel to $\vec{w}_i$ and the line connecting $\vec{x}_{i+\frac{1}{2}}$ and $\vec{x}_{i+1}$ has to be parallel to $\vec{w}_{i+1}$. The grid is called K-orthogonal if this is the case for all the cells. That is, if the flux over every edge in the cell can be approximated by a TPFA method, then the grid is K-orthogonal [Aavatsmark2007].

4.3 Multi-point-flux-approximation method (MPFA)

Having a K orthogonal mesh is not always possible due to certain constraints of the problem. However, if the mesh doesn't deviate too much from being K-orthogonal it is still possible to make an approximation of the fluxes. As in the TPFA method potential differences will be used to approximate the fluxes, however, more than two points are needed for the approximations, thereby the name MPFA.
The MPFA method can be used on several different meshes, but here it will be derived on a quadrilateral mesh with a version of the MPFA called the O-method [Aavatsmark2002].

Fig. (9) will help for the explanation of the idea

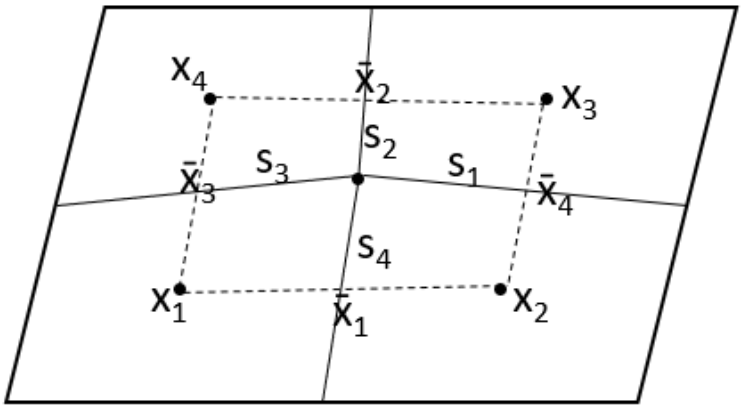

Figure 9: control cell made from the midpoints of 4 cells, figure adapted from [Aavatsmark2007]

The figure shows 4 cells of a mesh, each with a node in the center X_k, $k = (1, 2, 3, 4)$ by drawing a line between the points a new cell is formed, which will be called the control cell. Where the points $\bar{X}_i$, $i = (1, 2, 3, 4)$ are the midpoints between two points X_k and

edges S_j, $j = (1, 2, 3, 4)$ connecting the cells within the control cell. So an edge S_j of a control cell will be half of an edge of the cell. The idea of the MPFA is to compute the flux over each edge S_j in the control cell, once that is complete, the process is repeated for every control cell within the mesh until the flux over every control cell edge S is approximated. Then the flux over the edges of two adjacent control cells are added in order to get the flux over the edge for the actual cell of the mesh. The computation of the flux over control edges S on the boundaries also works as long as there is homogeneous Neumann boundary conditions. Outside the boundary cell an artificial cell is put with vanishing permeability, and the computation of the flux over the edge S can be done in the same way as earlier.

As an example, look at Fig. (10)

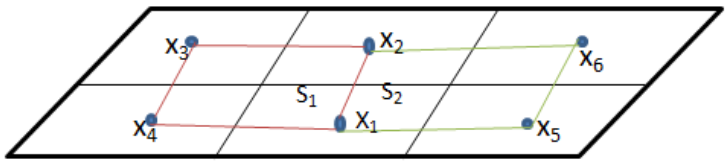

Figure 10: two control cells in 6 cells

it has 6 cells with 2 control cells, one formed between the center points x_1, x_2, x_3 and x_4 and the other one between x_1, x_2, x_5 and x_6. In order to get the flux over the edge from point x_1 to x_2 the flux over the edges of the control cells need to be computed and then adding the two cells S_1 and S_2 which combined will make up the edge S between point x_1 and x_2. Therefore 6 cells are needed in order to compute the flux over an edge between two cells.
The potential p in the cell center will be $p = p(x_i)$ and on the midpoint of the edges will be $\bar{p} = p(\bar{x}_i)$. The flux continuity equations over the edges can be expressed as:

$$\nabla \bar{p}_i \cdot \vec{w}_i = -\nabla \bar{p}_i \cdot \vec{w}_i \tag{73}$$

while the pressure continuity in the midpoints $\bar{p}$ can be written as

$$p_i + \nabla p_i(\bar{x}_i - x_i) = -(p_j + \nabla p_j(\bar{x}_j - x_j)), \tag{74}$$

where x_i and x_j are points in adjacent cells.

The equations can be put together in a matrix as such:

$$\begin{bmatrix} W & 0 \\ D & I \\ 0 & I \end{bmatrix} \begin{bmatrix} \nabla P \\ P \end{bmatrix} = \begin{bmatrix} 0 \\ 0 \\ I \end{bmatrix} \tag{75}$$

where W are all the $\vec{w}_i$ vectors, D are all the displacements $(\bar{x}_i - x_i)$ and I is the identity matrix. Eq. (75) displays pressure and flow continuity for a unit of pressure change imposed in the last row of eq. (75)

After the fluxes for the whole cell are found they can be used in a discrete variation of equation (67) to get an expression as

$$q_1 + q_2 - q_3 - q_4 = fV, \tag{76}$$

where V is the volume of the cell, f is assumed constant, and the fluxes of the following figure has been used as an example. By doing this process for every cell, and adding the fluxes together will result in the flux for the entire domain.

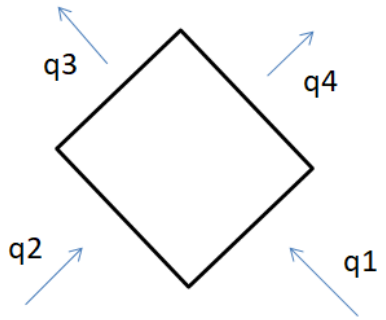

Figure 11: flux in and out of a cell

The MPFA method will result in a differential equation for the flux with the potential in the cell center as the unknown [Aavatsmark2007].

4.4 Multi-point-stress-approximation method (MPSA)

The MPSA is a method similar to the MPFA, howevever what is computed is very specific. The MPSA method approximates the stresses based on the gradient of the displacements. As this is the main numerical method used in this thesis, a more thorough explanation will be given. An explanation of the grid structure will also be given to fully understand the method and its applications [Nordbotten2014], [Keilegavlen and Nordbotten2017]. The following description is inspired by [Ucar et al.2018b].

4.4.1 Grid Structure

The domain Ω is partitioned into polyhedral cells Ω_i called control cells. A requirement of the grid is that it conforms to all fracture lines and faces. An edge shared between cells i and j is denoted by $S_{i,j}$. Furthermore, the control cells are partitioned further into subcells forming around each node of the control cell, and stretching out to the cell center

displacements of all neighbouring control cells, forming an interaction region. A subcell around node k in cell l is denoted by $\Omega_{l,k}$. As a result of this, the edges will be split into two, and $S_{c,l,k}$ will denote the edge between subcells l and c with k being the node associated with the subface.

The mesh is illustrated in the following figure, where the white dots are the vertices, and the black ones represent the unknown cell center locations.

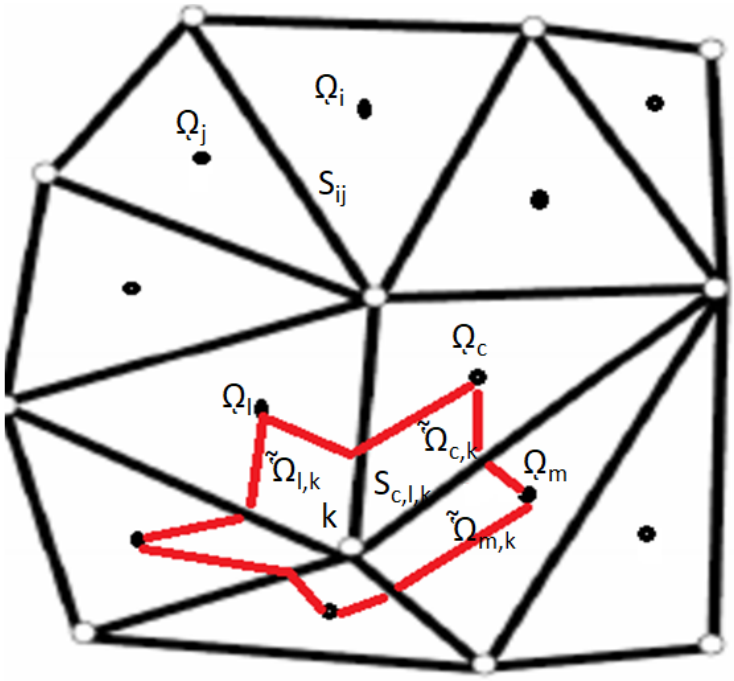

Figure 12: mesh of domain, figure adapted from [Ucar et al.2018b]

The fractures will be defined as line pairs in a 2-D domain and the two sides of the fracture will be defined as + and -. The traction on the fracture will in the same manner be defined as T_+ on the positive side and T_- on the negative side. Furthermore, each traction vector has a normal and shear component as depicted in the figure

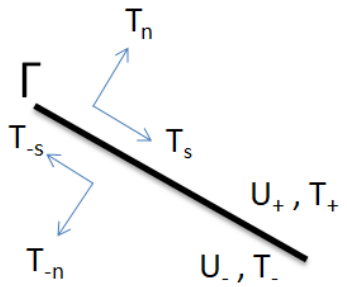

Figure 13: Fracture, figure adapted from [Ucar et al.2018b]

Due to the continuity and equilibrium condition the traction forces should be equal on both sides of the fracture. The relation between the traction forces on the fracture can be expressed as

$$T_+(n_+) = -T_-(n_-). \tag{77}$$

4.4.2 Construction of the problem

Instead of the general conservation problem (67) the MPSA solves specifically the momentum conservation problem

$$\int_{\Omega_i} \nabla \cdot \boldsymbol{\sigma} \, dV = -\int_{\Omega_i} \vec{b} \, dV \tag{78}$$

by using the divergence theorem on the left hand side, the problem may be written as

$$\int_{\partial\Omega_i} \vec{T} \, dA = \sum_j \int_{S_{i,j}} \vec{T} \, dA = -\int_{\Omega_i} \vec{b} \, dV, \tag{79}$$

Ω_i is the control cell and $S_{i,j}$ are the edges between cell i and its surrounding cells j. Alternatively stated, it is all the edges for the boundary $\partial\Omega_i$.
The traction between cells i and j is introduced as $T_{i,j}$ being the traction over the edge $S_{i,j}$, eq. (79) can then be written as

$$-b_i = \frac{1}{|\Omega_i|} \sum_j T_{i,j}. \tag{80}$$

To be able to define the traction $T_{i,j}$, a definition of the displacement within each subcell is necessary. There is a linear approximation of the displacement within each subcell $\Omega_{i,k}$ which defines the discrete displacements in the whole domain as

$$\vec{u} = u_i + \nabla u_{i,k}(x - x_i), \tag{81}$$

where $u_i = u(x_i)$ is the cell center displacement and x_i is the coordinates of the cell center, x is a point within the subcell $\Omega_{i,k}$ and $\nabla u_{i,k}$ is the gradient of the displacement within the subcell $\Omega_{i,k}$.

The MPSA method defines the traction $T_{i,j}$ between cells i and j, as a linear function of the cell-center displacements u_i such that

$$T_{i,j} = \sum_k t_{i,j,k} u_k \tag{82}$$

where $t_{i,j,k}$ is the traction weight tensor and k denotes the cells that are neighbors to edge $S_{i,j}$. Going even further, with each subface $S_{i,j,l}$ there is a corresponding traction weight tensor denoted as $\bar{t}_{i,j,l,k}$. This means that the traction weight tensor $t_{i,j,k}$ for each face $S_{i,j}$ can be calculated as the sum of the contribution of the traction weight tensors $\bar{t}_{i,j,l,k}$ from each subface $S_{i,j,l}$

$$t_{i,j,k} = \sum_l \bar{t}_{i,j,l,k}. \tag{83}$$

The calculation of the traction weight tensors and the rest of the MPSA method will be done by first solving a local linear problem defined on each subcell for a node l and then later solve a global problem defined on each cell.

4.4.3 Local linear system

To generate the local linear system, two continuity equations are necessary; the continuity of the traction, and displacement over the edges.
Continuity of traction over a subface is

$$T_{i,j,l} = -T_{j,i,l}. \tag{84}$$

Recalling that $T = \boldsymbol{\sigma} \cdot \vec{n}$ and defining the discrete stress $\boldsymbol{\sigma}$ in terms of Hooke's law:

$$\boldsymbol{\sigma_{i,l}} = \frac{1}{2}[\mathbb{C}_i : \nabla u_{i,l} + (\mathbb{C}_i : \nabla u_{i,l})^T], \tag{85}$$

equation (84) may be written as

$$[\mathbb{C}_i : \nabla u_{i,l} + (\mathbb{C}_i : \nabla u_{i,l})^T] \cdot \bar{n}_{i,j,l} = -[\mathbb{C}_j : \nabla u_{j,l} + (\mathbb{C}_j : \nabla u_{j,l})^T] \cdot \bar{n}_{j,i,l}, \tag{86}$$

where $\mathbb{C}$ is a 4th order stiffness tensor and $\bar{n}_{i,j,l}$ is the area weighted normal vector for the corresponding subface.
The continuity of displacement can be written as

$$u_i + \nabla u_{i,l}(\bar{x}_{i,c,l} - x_i) = u_j + \nabla u_{j,l}(\bar{x}_{i,c,l} - x_j), \tag{87}$$

where $\bar{x}_{i,c,l}$ is the calculated continuity point, which is located one third the distance from the face center to the node l.

The linear system for each node in the grid may be expressed as follows by combining equations (86) and (87)

$$\begin{bmatrix} n^T\mathbb{C} & 0 \\ D_G & D_U \\ 0 & I \end{bmatrix} \begin{bmatrix} \nabla U \\ U^\Omega \end{bmatrix} = \begin{bmatrix} 0 \\ 0 \\ I \end{bmatrix}. \tag{88}$$

Here ∇U represents the gradients associated with the interaction region, D_G contains the distances from the cell centers to the continuity points, D_U is the matrix of ± 1 representing the contributions from cell centers in equation (87), U^Ω represents the cell-center displacement, and I is the identity matrix.

By solving this system for the subcell gradients ∇U, the linear system gives the local deformation response to a unit displacement of each of the cell center variables because U^Ω in (88) imposes unit displacement. Inserting the solution of the subcell gradients ∇U into equation (85) will give the discrete stress in the subcell, which can be used in eq. (83) and (82) to get the traction between subcells i and j as a linear function of cell center displacements.

4.4.4 Global linear system

The global system can now be solved by solving the local linear system for each node in the cells, which will give the traction vectors of eq. (82) in their desired form. Moreover, this results in a discrete expression for the balance of momentum equation for each cell Ω_i. Combining the equations for each cell without fractures will result in the following expression:

$$-b_i = \frac{1}{|\Omega_i|} \sum_j T_{i,j} = \frac{1}{|\Omega_i|} \sum_j \sum_k t_{i,j,k} u_k, \tag{89}$$

by defining $\phi^\Omega = \sum_j \sum_k t_{i,j,k}$ and neglecting body forces b_i the above equation can be written as

$$\phi^\Omega U^\Omega = 0. \tag{90}$$

4.4.5 MPSA with a fracture

The need to include a fracture into the local linear system arises, which can be done by first defining a fracture, where the fracture is defined as being between two cells. Further-

more, two displacement values are defined in the center of the edge on each side of the fracture as shown in Fig. (14).

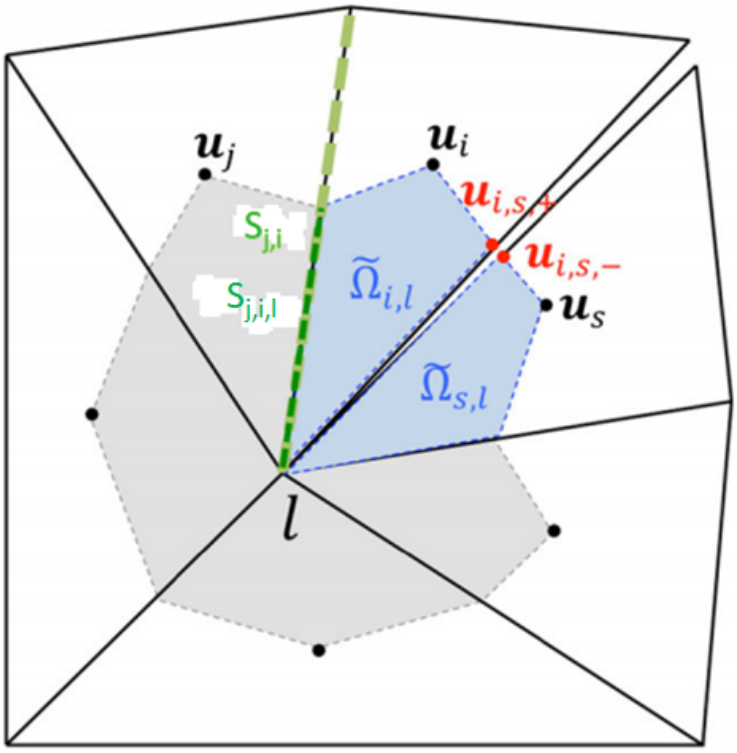

Figure 14: fracture between two subcells, figure adapted from [Ucar et al.2018b]

The displacements on each side of the fracture faces can be described as follows

$$u_{i,s,+} = u_i + \nabla u_{i,l}(\bar{x}_{i,c,l} - x_i) \tag{91}$$

$$u_{i,s,-} = u_s + \nabla u_{s,l}(\bar{x}_{s,c,l} - x_s), \tag{92}$$

where $\bar{x}_{i,c,l}$ and $\bar{x}_{s,c,l}$ are the split continuity points on subfaces $\bar{S}_{i,c,l}$ and $\bar{S}_{s,c,l}$.

Including these displacement conditions into the previous local linear system (88) results in a new local linear system with a fracture

$$\begin{bmatrix} n^T\mathbb{C} & 0 & 0 \\ D_G & D_U & 0 \\ D_G^\Gamma & I & -I \\ 0 & I & 0 \\ 0 & 0 & I \end{bmatrix} \begin{bmatrix} \nabla U \\ U^\Omega \\ U^\Gamma \end{bmatrix} = \begin{bmatrix} 0 \\ 0 \\ 0 \\ I \\ I \end{bmatrix}, \tag{93}$$

where D_G^Γ is the distance from the center of the cells that have internal boundaries to the continuity points. So the third row represents the internal boundary condition displacements for the fracture faces eq. (91), eq. (92) and U^Γ represents the internal displacements, that is, the displacement on the positive and negative side of the fracture faces. As before, the two last rows imposes a unit displacement in each cell center and fracture face.

By solving (93) for $\nabla U, U^\Omega$ and U^Γ results in an expression with the displacement gradient in terms of the cell center displacement, and displacement on the fracture faces. Furthermore, using this expression as before inside eq. (85) will give the discrete stress in the subcell, which can be used in eq. (83) and eq. (82) to get the traction between subcells i and j as a linear function of cell center and fracture displacements.

Including fractures will result in a more complicated expression, recalling the traction continuity on the fractures eq. (77) which can be expressed with eq. (82), eq. (83) and eq. (85). The traction for each edge of a cell can be found by adding every contribution of the traction of the edges of subcells which form the complete edge of the cell. The traction weight tensor on the positive side of a fracture, $\sum_k t_{i,s,+,k}$ can then be written as

$$\bar{P} = [\bar{P}^\Omega, \bar{P}_+^\Gamma, \bar{P}_-^\Gamma], \tag{94}$$

where $\bar{P}^\Omega$ is the traction weight tensor on the edge of the cell, while $\bar{P}_+^\Gamma$ and $\bar{P}_-^\Gamma$ is the traction weight tensor on the positive and negative sides of the fracture.

Moreover, the total displacement of U is a combination of the cell-center displacement and the displacement on the positive and negative sides of the fracture, $U = [U^\Omega, U_+^\Gamma, U_-^\Gamma]^T$. The traction vector on the positive side of the fracture face may then be written as

$$[\bar{P}^\Omega, \bar{P}_+^\Gamma, \bar{P}_-^\Gamma]U = 0. \tag{95}$$

The equilibrium condition between the negative and positive side of the fracture can be written as

$$[\bar{t}^\Omega, \bar{t}_+^\Gamma, \bar{t}_-^\Gamma]U \tag{96}$$

where

$$\bar{t} = [\bar{t}^\Omega, \bar{t}_+^\Gamma, \bar{t}_-^\Gamma] \tag{97}$$

represents the summation of the traction weight tensor between positive and negative fracture faces ($\sum_k t_{i,s,+,k} + \sum_k t_{i,s,-,k}$).

The global system, eq. (90), including fractures and the continuity of the stress on each side of the fracture faces can now be formulated as

$$\begin{bmatrix} \phi^\Omega & \phi_+^\Gamma & \phi_-^\Gamma \\ \bar{t}^\Omega & \bar{t}_+^\Gamma & \bar{t}_-^\Gamma \end{bmatrix} U = \begin{bmatrix} 0 \\ 0 \end{bmatrix}, \tag{98}$$

where the first row is the force balance equations for each cell in the grid, while the second row is the continuity of the stresses between each side of the fracture [Ucar et al.2018b].

A simplified recap of the MPSA method would be that it solves the momentum balance equation by first solving for the displacement U in the subcells for the local problem and then using the displacement gradients ∇U to have an expression for the traction $T_{i,j}$ on each cell, followed by summing all tractions for every cell, to get the traction over the entire domain, which will be equal to the divergence of the stress, $\nabla \cdot \boldsymbol{\sigma}$.

5 Simulations and Results

5.1 Convergence Test

A convergence test has been done in order to make sure that the solutions of the numerical simulations actually converge, and also to identify a suitable mesh resolution for the simulations. A convergence test has been done for the displacement and traction.
The convergence test was done numerically by referring to a test problem where an analytical solution was manufactured. Recalling that the problem

$$\nabla \cdot \boldsymbol{\sigma}_{bc} = f \tag{99}$$

is solved, where $\boldsymbol{\sigma}_{bc}$ is the internal stress tensor for the test problem, defined by Hooke's law

$$\boldsymbol{\sigma}_{bc} = \begin{bmatrix} 2G\frac{\partial u_{0x}}{\partial x} + \lambda(\nabla \cdot \vec{u}) & G(\frac{\partial u_{0x}}{\partial y} + \frac{\partial u_{0y}}{\partial x}) \\ G(\frac{\partial u_{0y}}{\partial x} + \frac{\partial u_{0x}}{\partial y}) & 2G\frac{\partial u_{0y}}{\partial y} + \lambda(\nabla \cdot \vec{u}) \end{bmatrix}. \tag{100}$$

The displacement is defined as non-linear functions

$$\begin{bmatrix} u_{0x} = \cos x - \sin y \\ u_{0y} = 2\sin x + \sin y \end{bmatrix} \tag{101}$$

therefore the source term will be the divergence of the stress

$$f = \nabla \cdot \boldsymbol{\sigma}_{bc} = \begin{bmatrix} \frac{\partial \sigma_{xx}}{\partial x} + \frac{\partial \sigma_{xy}}{y} \\ \frac{\partial \sigma_{yx}}{x} + \frac{\partial \sigma_{yy}}{y} \end{bmatrix}. \tag{102}$$

Now a simulational problem with boundary conditions equal to the analytical solution and with the same source term f will be introduced

$$\nabla \cdot \bar{\boldsymbol{\sigma}}_{bc} = f, \tag{103}$$

where $\bar{\boldsymbol{\sigma}}_{bc}$ is the stress tensor for the simulational problem, where the displacement functions in eq. (101) are used when setting the dirichlet boundary conditions. The domain is defined in meters as $\Omega = [0,1] \times [0,1]$ and the fracture plane is defined as $\Gamma = [\frac{1}{6}, \frac{1}{2}], [\frac{5}{6}, \frac{1}{2}]$. The contact mechanics problem related to the fracture is not solved here, and the fracture plane Γ is therefore not affecting the solution. The fracture is simply used for the computation of the slip tendency on the fracture.

Since the simulational problem has the same source term f as the test problem and the boundary condition displacements for the simulational problem uses the displacement

functions defined for the test problem, the solutions should be almost identical if the MPSA method used for the simulational problem is correct and should get better and better as the mesh is refined
This is seen to be the case, and is shown for the traction and displacement on the whole domain with a log-log plot.

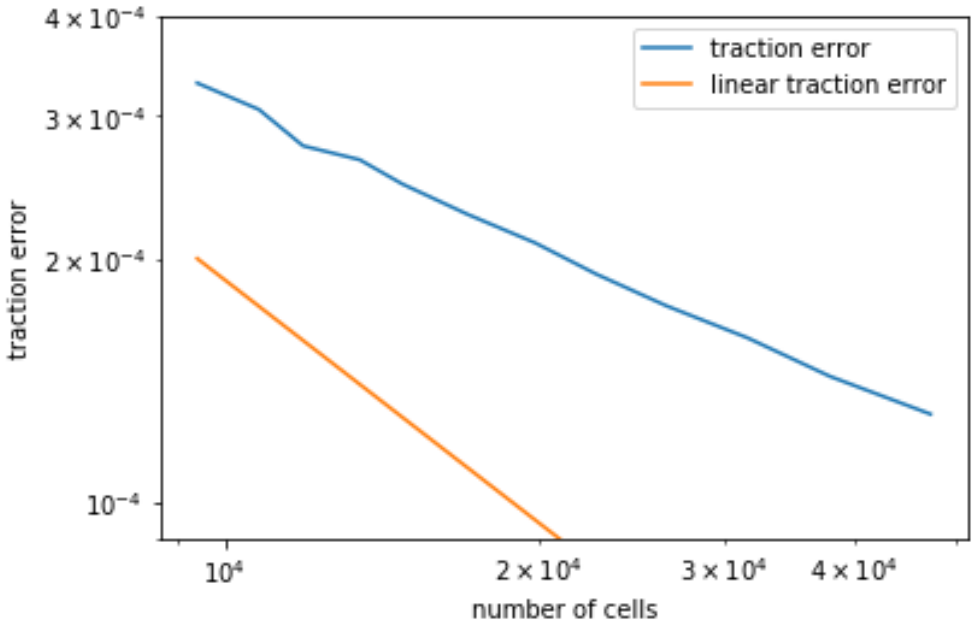

Figure 15: convergence of the MPSA method for the traction on the whole domain

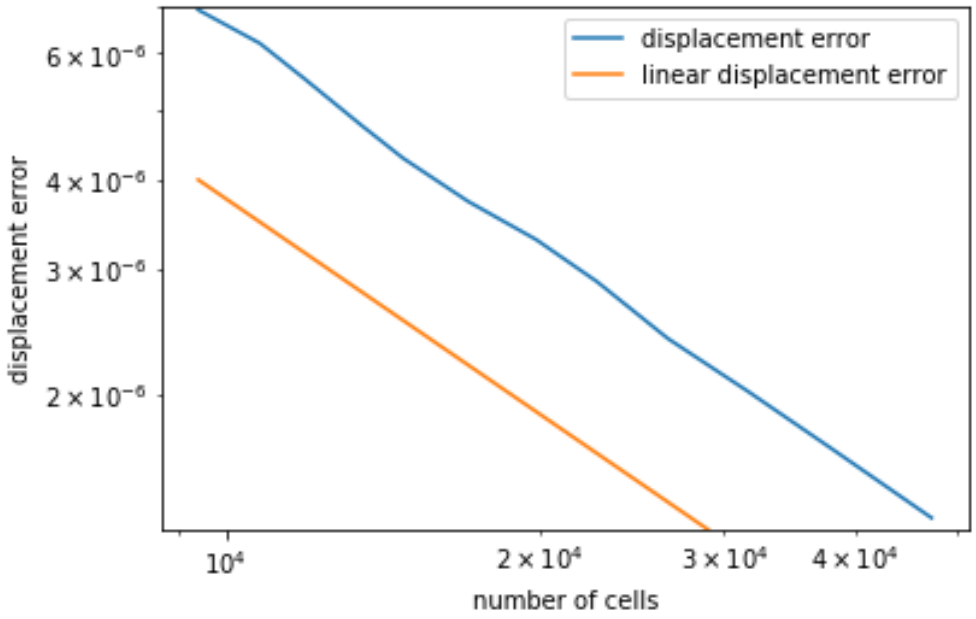

Figure 16: convergence of the MPSA method for the displacement on the whole domain

The error shown in Fig. 16 are the relative errors, which for the traction would be

$$\epsilon_t = \frac{|T_{ex} - T_{approx}|}{|T_{ex}|}, \tag{104}$$

where T_{ex} is the exact traction and T_{approx} is the approximate traction. The tractions are weighted by the square of the face areas, and the displacement relative error would be

$$\epsilon_u = \frac{|u_{ex} - u_{approx}|}{u_{ex}}, \tag{105}$$

where u_{ex} is the exact displacement, u_{approx} is the approximate displacement and all the displacements are weighted by the cell areas.

As can be seen from Fig. 15 and Fig. 16, the relative errors for the traction and displacement are low regardless of mesh size. The following simulations will use a mesh size of around 15 000 cells for convenience.

5.2 Model problem for the simulations

The following simulations will look at the slip tendency for a single closed one dimensional fracture line within a two dimensional plane. These domains will be acted on by an inter-

nal stress field due to prescribed boundary conditions and an isotropic background stress field set to be $\sigma_{11} = \sigma_{22} = 0.12$ MPa.

Young's modulus, E is set to be 37.7GPa and Poisson's ratio is 0.26 as was found for rocks with temperatures of $50C^{\circ}$ [Liu and Xu2015].

The slip tendency is calculated with the use of the MPSA method for the general stress equilibrium equation

$$\begin{aligned} \nabla \cdot \boldsymbol{\sigma}_{bc} &= 0 \ \ in \ \ \Omega \\ \boldsymbol{\sigma}_{bc|\partial\Omega_n} &= \vec{t}_n. \\ \vec{u}_{|\partial\Omega_d} &= \vec{u}_d \end{aligned} \tag{106}$$

The aim of the thesis is to compute the slip tendency on the fracture in order to know the likelihood of slip to occur. The internal stress $\boldsymbol{\sigma}_{bc}$ from the boundary conditions gets computed in order to find the slip tendency on the fracture.

recalling the general stress-strain relationship (eq. 36) and the strain-displacement (eq. 37)

the strain will be solved for by approximating the displacements numerically with the use of the MPSA method covered in the next chapter. By having the strains $\mathcal{E}$ the stress $\boldsymbol{\sigma}_{bc}$ can be found with the use of eq. (36).

After the stress tensor $\boldsymbol{\sigma}_{bc}$ is found the superposition (eq. 58) of the background stress $\boldsymbol{\sigma}_{bs}$ and $\boldsymbol{\sigma}_{bc}$ yields the complete stress $\boldsymbol{\sigma}$. The tractions on the fracture can then be computed as

$$\vec{T} = \boldsymbol{\sigma} \cdot \vec{n} \tag{107}$$

where $\vec{n}$ is the normal vector on the fracture. Afterwards the traction vector gets decomposed into its normal and shear directions, and so the slip tendency on the fracture can be computed as $ST = \frac{|T_s|}{|T_n|}$

The domain will be a two dimensional plane $\Omega = [0, n] \times [0, n]$ km where $n \in \mathbb{R},\ n > 0$ with a fracture line Γ located somewhere in the center of the domain. The fractures, whether they are open or closed can be modelled as straight lines since the magnitude of their aperture is way smaller than their length in the model problem. The domain is generated as a triangular mesh with the use of GMSH which is a mesh generator that Porepy uses.

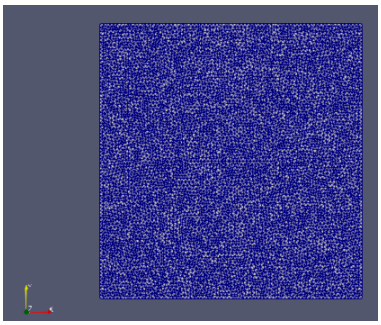

Figure 17: generated mesh of the domain

It should also be noted that the stress will be dependent on the temperature due to the fact that Young's modulus E is dependent on temperature. It is seen that lame's parameters are as well since both lame's parameters are dependent on E (recall eq. 43 and eq. 44). By knowing the lame's parameters, the 4th order stiffness tensor $\mathbb{C}$ can be computed which in turn means that the stress tensor $\boldsymbol{\sigma}$ is dependent on temperature due to (eq.36). It should be noted that the slip in itself is not modeled, and so secondary consequences of slip such as slip avalanches are not considered.

For the first simulation the domain is defined as $\Omega = [0, 3] \times [0, 3]\ km$ and the fracture line in the beginning is set to be $\Gamma = [1, 1.5], [2, 1.5]$ km as depicted in Fig. 18

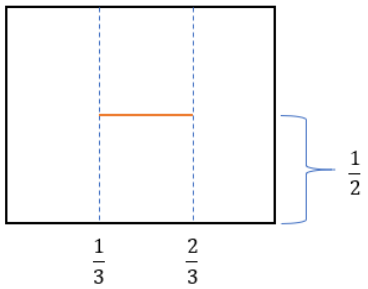

Figure 18: location of the fracture plane with normalized units

First a simulation is done to see how much the slip tendency is affected by the mesh refinement

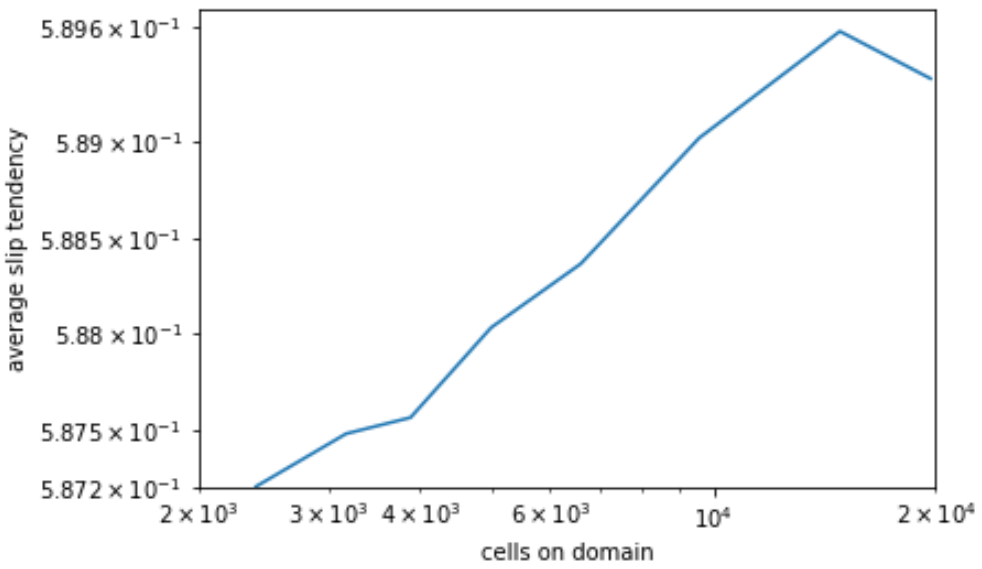

Figure 19: slip tendency vs number of cells

As can be seen from Fig. 19, the difference in the value of the slip tendency from 2500 cells to 20000 cells is less than 1%. Any mesh refinement would therefore be sufficient, but 15000 will be used just to be absolutely certain, as the computation is very fast in 2-D regardless.

5.3 Slip tendency as a function of the orientation of the fracture

5.3.1 Pure shear test with isotropic BS

The first simulation will look at how the slip tendency on the fracture will change according to the orientation of the fracture within the domain. The boundary conditions

$$\vec{U_0} = [u_{0x}, u_{0y}] \tag{108}$$

are set to be Dirichlet on the top and bottom surfaces while neumann on the left and right surfaces. The top surface will have 1.5cm displacement tangentially, i.e $u_{ox} = 1.5$cm. The bottom surface will be fixed with 0 displacement and the left and right surfaces will have 0 forces as depicted by Fig. (20) (setup #1).

The background stress (BS) is isotropic and set to be $\sigma_{11} = \sigma_{22} = 0.12$ MPa.

The orientation will go counterclockwise about the midpoint of the starting location of the fracture [1.5,1.5] km. The rotation will go from $0 - 90°$ with $15°$ increments about the x-axis.

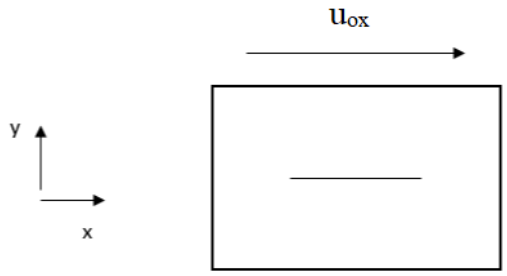

Figure 20: shear test

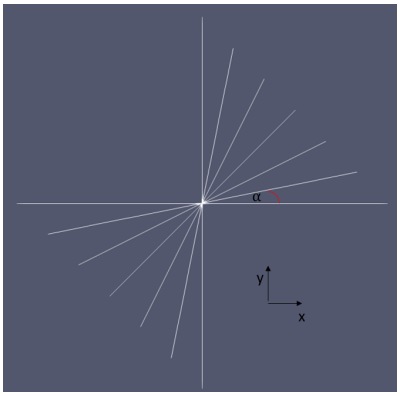

Figure 21: orientation of fractures

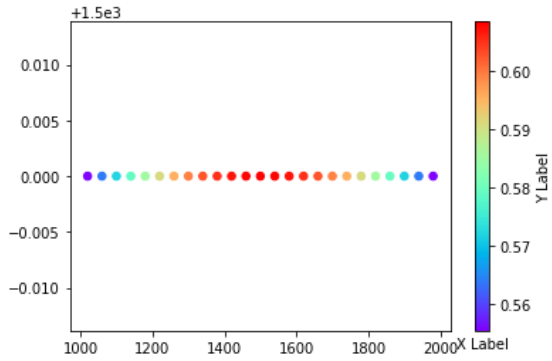

Figure 22: ST on 0° rotated fracture for setup# 1 with isotropic BS

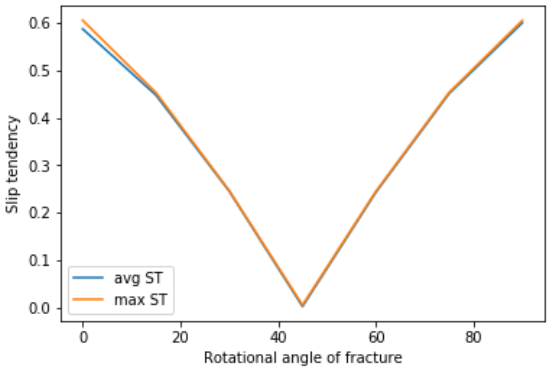

Figure 23: ST vs angle of the fracture for setup #1 with isotropic BS

Here the MPSA method has computed the tractions on the fracture surface directly. The slip tendency has then been computed as the ratio between the shear and normal tractions $ST = \frac{|T_s|}{|T_n|}$. On Fig. 22 the slip tendency is computed in each point of the fracture, whereas in Fig. 23 the average slip tendency is computed. The average is computed as sum of the slip tendency in each point as in Fig. 22 divided by the number of points.

$$ST_{avg} = \frac{1}{N} \sum_{n=1}^{N} ST_n \tag{109}$$

where N is the number of points.

The shape of the figure can be seen to be symmetric around the angle of 45°. Having the highest slip when the fracture is planar or 90° and seen to be lowest at 45°. The slip tendency is highest at the beginning, since the highest shear traction and lowest normal traction on the fracture occurs here. The slip tendency tends downward from $0 - 45°$ as the normal traction increases and shear traction decreases until the slip reaches its lowest

value at 45°. Afterwards, the slip tendency increases again as the normal tractions decrease and the shear tractions increase until the slip tendency is identical to when the fracture was planar. This is shown visually in the following figure; displaying the normal tractions T_n and shear tractions T_s.

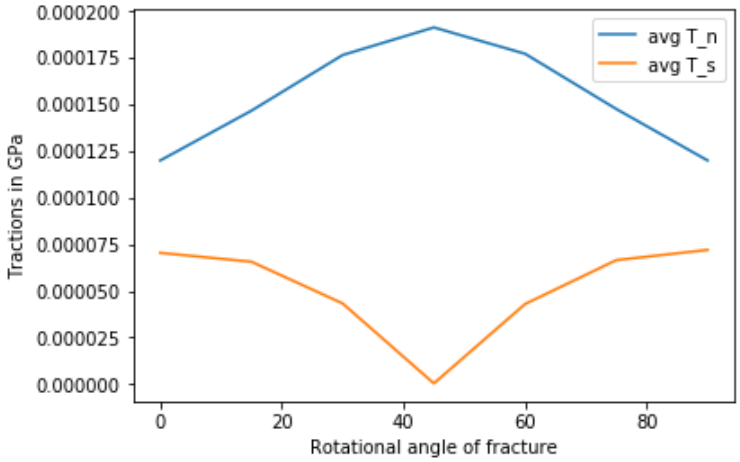

Figure 24: traction vs orientation for setup # 1 with isotropic BS

To better understand the nature of the normal and shear tractions for this simulation, recall the stress tensor $\boldsymbol{\sigma}$ for linear elasticity

$$\boldsymbol{\sigma} = 2G\mathcal{E} + \lambda tr(\mathcal{E})I, \tag{110}$$

where $\mathcal{E} = \frac{1}{2}(\nabla u + \nabla u^T)$. The deformation for the shear test can be visualized as depicted in Fig. 25

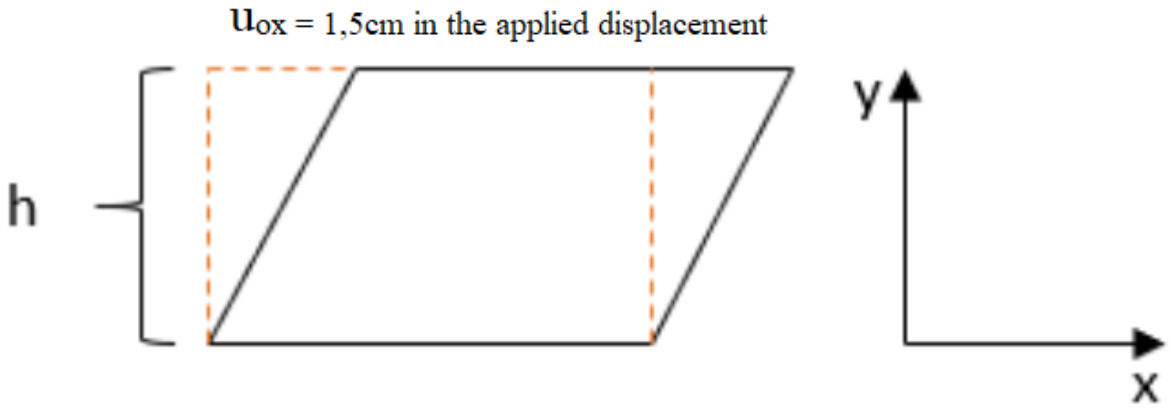

Figure 25: illustrative deformation of domain for setup #1

This can be seen from Fig. 26 which shows the displacement in the x direction u_{0x}

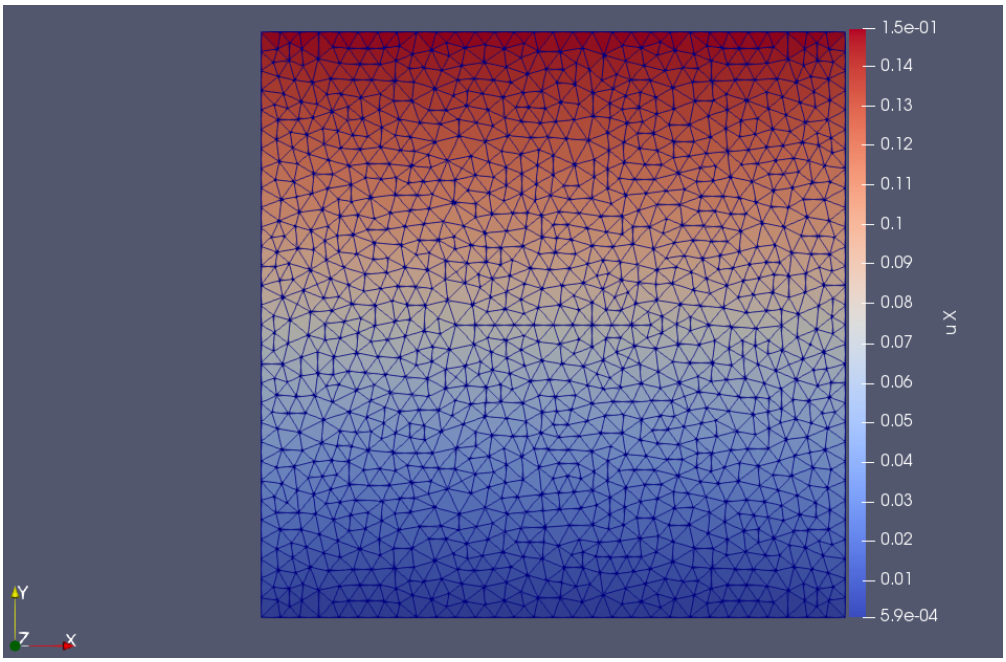

Figure 26: Displacement in the X-direction for setup # 1

As can be seen from Fig. 26 the displacement u_{0x} changes only as a function of y, it is slightly dependent on x, but its so small that it is negligible. The second Fig. 27 shows the displacement in the y direction u_{0y}

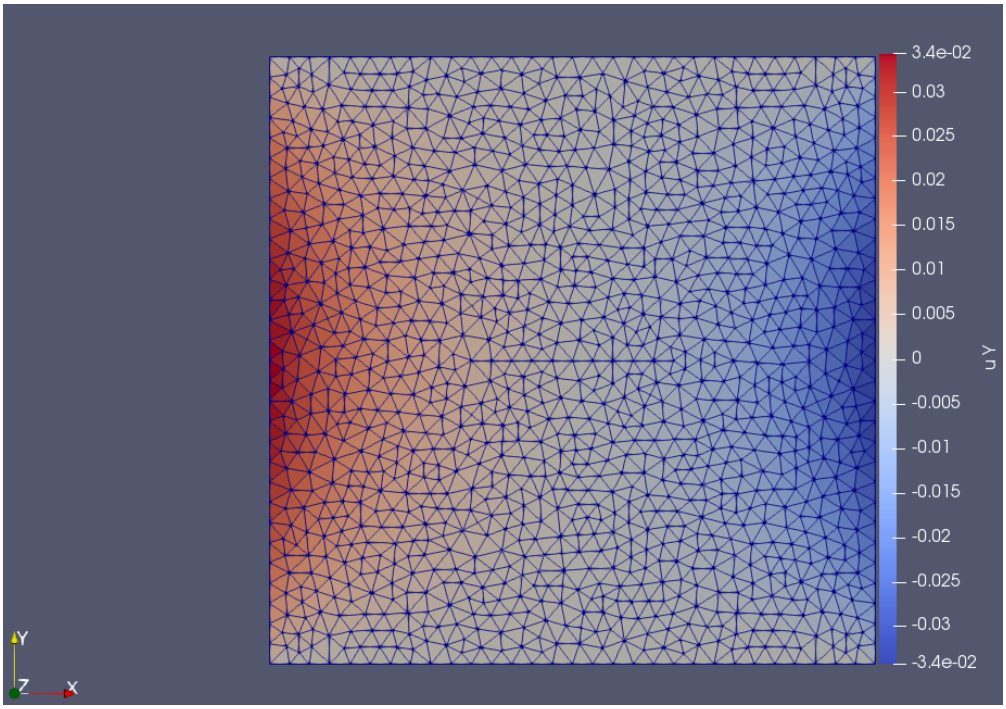

Figure 27: Displacement in the Y-direction for setup # 2

As can be seen from Fig. 27, the displacement is very close to zero, and is especially close to zero in the area where the fracture lies. It is therefore safe to assume a small displacement ϵ in the y direction.

Based on Fig. 26 and Fig. 27 an approximation for the displacement happening to the domain will be given by $\vec{u} = [Ly, \epsilon]$ where $L = \frac{u_{0x}}{h}$, h is the height of the domain and ϵ is a very small value.

Due to the symmetry of the displacement within the domain it seems like the derivative in the y-direction is extremely small. Taking the gradient of the displacement it follows then that

$$\nabla u = \begin{bmatrix} 0 & L \\ 0 & 0 \end{bmatrix} \; and \; \nabla u^T = \begin{bmatrix} 0 & 0 \\ L & 0 \end{bmatrix} \tag{111}$$

such that

$$\boldsymbol{\sigma} = \begin{bmatrix} 0 & LG \\ LG & 0 \end{bmatrix} \tag{112}$$

since the second term will be zero, i.e $trace(\mathcal{E}) = 0$.

The stress field will be due to both the background stress and the internal stress generated by the boundary conditions. The tractions will therefore be a superposition of these two

contributions. The traction can be expressed as $\vec{T} = \vec{T}_{bc} + \vec{T}_{bs}$, where $\vec{T}_{bc} = \boldsymbol{\sigma} \cdot \vec{n}$ is the traction due to the internal stress and $\vec{T}_{bs}$ is the traction due to the background stress.

The traction due to the boundary conditions will be calculated first and can be expressed as

$$\vec{T}_{bc} = \begin{bmatrix} 0 & LG \\ LG & 0 \end{bmatrix} \begin{bmatrix} n_x \\ n_y \end{bmatrix} = \begin{bmatrix} LGn_y \\ LGn_x \end{bmatrix}, \tag{113}$$

the normal traction will be

$$T_n^{bc} = \vec{T}_{bc} \cdot \vec{n} = \begin{bmatrix} LGn_y & LGn_x \end{bmatrix} \begin{bmatrix} n_x \\ n_y \end{bmatrix} = LGn_y n_x + LGn_x n_y = 2LGn_x n_y, \tag{114}$$

and the shear traction vector will be

$$\vec{T}_s^{bc} = \vec{T}_{bc} - T_n^{bc} \cdot \vec{n} = \begin{bmatrix} LGn_y \\ LGn_x \end{bmatrix} - \begin{bmatrix} 2LGn_x^2 n_y \\ 2LGn_x - 2LGn_x n_y^2 \end{bmatrix} = \begin{bmatrix} LGn_y(1-2n_x^2) \\ LGn_x(1-2n_y^2) \end{bmatrix}, \tag{115}$$

finally the shear traction can be expressed as

$$T_s^{bc} = \sqrt{(LGn_y(1-2n_x^2))^2 + (LGn_x(1-2n_y^2))^2}. \tag{116}$$

The computation of the tractions T_{bs} due to the background stress will be computed similarly except that the stress tensor $\boldsymbol{\sigma}_{bs}$ will be different

$$\boldsymbol{\sigma}_{bs} = \begin{bmatrix} \sigma_{11} & 0 \\ 0 & \sigma_{22} \end{bmatrix}, \tag{117}$$

resulting in the traction being

$$\vec{T}_{bs} = \begin{bmatrix} \sigma_{11} & 0 \\ 0 & \sigma_{22} \end{bmatrix} \begin{bmatrix} n_x \\ n_y \end{bmatrix} = \begin{bmatrix} \sigma_{11} n_x \\ \sigma_{22} n_y \end{bmatrix}, \tag{118}$$

and the normal traction becoming

$$T_n^{bs} = \vec{T}_{bs} \cdot \vec{n} = \sigma_{11} n_x^2 + \sigma_{22} n_y^2, \tag{119}$$

the shear traction becomes

$$T_s^{bs} = \sqrt{(n_x[\sigma_{11} - \sigma_{11} n_x^2 + \sigma_{22} n_y^2])^2 + (n_y[\sigma_{22} - \sigma_{11} n_x^2 + \sigma_{22} n_y^2])^2}. \tag{120}$$

However since this is an isotropic case

$$\sigma_{11} = \sigma_{22} \implies T_n^{bs} =_{11} n_x^2 +_{22} n_y^2 = \sigma_{11}(n_x^2 + n_y^2) = \sigma_{11} \tag{121}$$

and

$$T_s^{bs} = 0. \tag{122}$$

Finally the shear and normal tractions as a superposition of the influences of the background stress and boundary conditions will be

$$\begin{aligned} T_s = T_s^{bc} + T_s^{bs} &= \sqrt{(LGn_y(1-2n_x^2))^2 + (LGn_x(1-2n_y^2))^2} + \sqrt{0^2} \\ &= \sqrt{(LGn_y(1-2n_x^2))^2 + (LGn_x(1-2n_y^2))^2} \end{aligned} \tag{123}$$

and

$$T_n = T_n^{bc} + T_n^{bs} = 2LGn_xn_y + \sigma_{11}. \tag{124}$$

To see if these approximated values match up with the numerical results a simulation was done plotting the approximated values as a function of θ with $\theta \in [0, 90]$ with 1° increments. This means that $n_x = \sin\theta$ and $n_y = \cos\theta$ in the equations for the shear and normals tractions. The first figure shows the approximated values of the normal and shear tractions vs the numerical, where the numerical values are as in Fig. 24 with 15° increments.

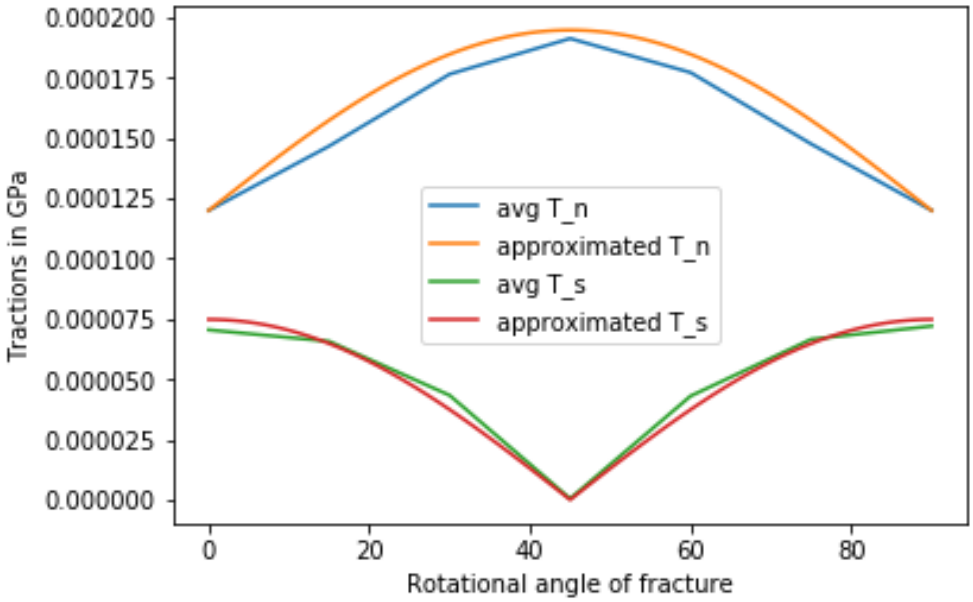

Figure 28: approximated vs numerical tractions for setup # 1 with isotropic BS

Fig. 29 shows the slip tendency

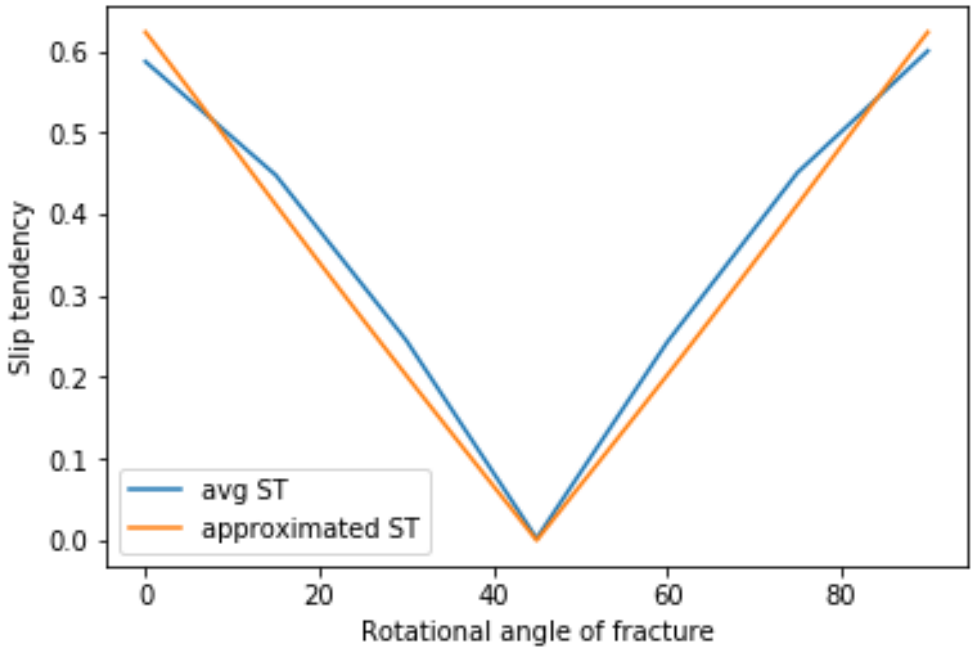

Figure 29: approximated vs numerical slip tendency for setup # 1 with is

As can be seen from Fig. 28 and Fig. 29 the approximated and numerical values match well. These plots can be explained by the equations. For instance, from eq. (123) it can be seen that the shear traction will be identical at 0° and 90° since for 0°, $n_x = 0$ and $n_y = 1$ which means that eq. (123) will reduce to

$$T_s = \sqrt{(LG)^2 + 0^2} = LG. \tag{125}$$

Likewise for 90° the opposite occurs, $n_y = 0$ and $n_x = 1$ resulting in

$$T_s = \sqrt{0^2 + (LG)^2} = LG. \tag{126}$$

Furthermore, it can be shown that the shear traction will indeed be 0 at 45° since then $n_x = n_y = \frac{\sqrt{2}}{2}$ which results in the eq. (123) becoming

$$T_s = \sqrt{2[(LGn_y(1 - 2n_y^2))^2]} \tag{127}$$

where the term $(1 - 2n_y^2)$ is 0 for $n_y = \frac{\sqrt{2}}{2}$ resulting in $\vec{T_s} = \vec{0}$.

Now for the explanation of the normal tractions in Fig. 28. As can be seen from eq. (124) the term $2LGn_xn_y$ will be 0 when the fracture line is oriented 0° and 90° since either $n_x = 0$ and $n_y = 1$ or the other way around. Resulting in $T_n = J$ which is the contribution from the background stress. The normal tractions will obtain its maximum at 45° since then $n_x = n_y$ and the term $2LGn_xn_y$ is maximized, resulting in $T_n = LG + \sigma_{11}$.

5.3.2 Pure shear test with anisotropic BS

What follows is the same simulation with an anisotropic background stress instead, where $\sigma_{11} = 0.12$ MPa and $\sigma_{22} = 0.4$ MPa.

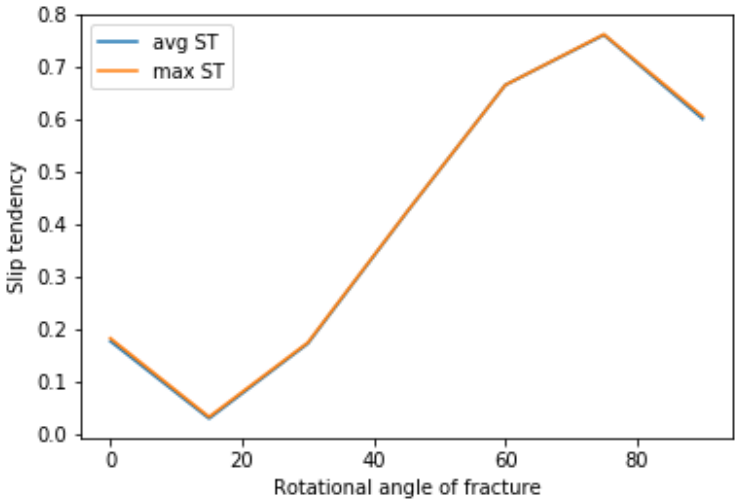

Figure 30: Slip tendency vs angle of the fracture for setup #1 with anisotropic BS

To better understand the results, it helps to look at the normal and shear tractions illustrated in Fig. 31.

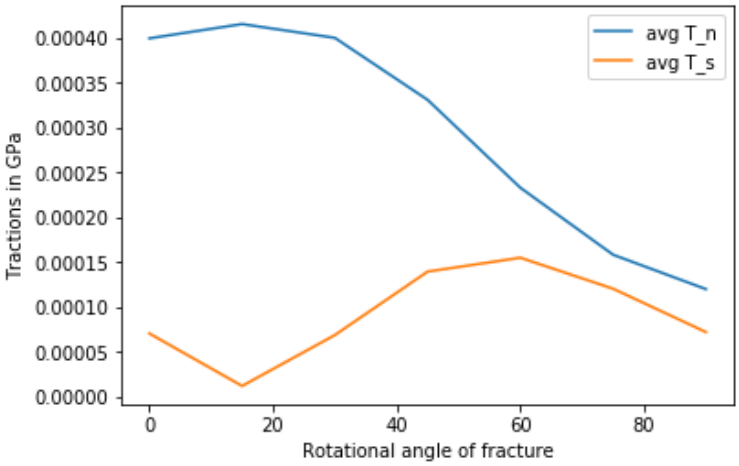

Figure 31: Traction vs angle of the fracture for setup # 1 with anisotropic BS

The results can be explained in the same way as earlier, but in this case $\sigma_{11} \neq \sigma_{22}$ such that T_n^{bs} and T_s^{bs} will be different.
That is, the normal traction will be eq. (119)

$$T_n^{bs} = \vec{T}_{bs} \cdot \vec{n} = \sigma_{11} n_x^2 + \sigma_{22} n_y^2 \tag{128}$$

and the shear traction will be eq. (120)

$$T_s^{bs} = \sqrt{(n_x[\sigma_{11} - \sigma_{11}n_x^2 + \sigma_{22}n_y^2])^2 + (n_y[\sigma_{22} - \sigma_{11}n_x^2 + \sigma_{22}n_y^2])^2}. \tag{129}$$

The final normal and shear tractions due to the superposition of the tractions of the boundary conditions and anisotropic background stress then becomes

$$T_n = T_n^{bc} + T_n^{bs} = 2LGn_xn_y + \sigma_{11}n_x^2 + \sigma_{22}n_y^2 \tag{130}$$

and

$$\begin{aligned} \vec{T_s} = T_s^{bc} + T_s^{bs} = \sqrt{(LGn_y(1-2n_x^2))^2 + (LGn_x(1-2n_y^2))^2} \\ +\sqrt{(n_x[\sigma_{11} - \sigma_{11}n_x^2 + \sigma_{22}n_y^2])^2 + (n_y[\sigma_{22} - \sigma_{11}n_x^2 + \sigma_{22}n_y^2])^2}. \end{aligned} \tag{131}$$

These approximated values has again been compared with the numerical values, and can be seen in Fig. 32 and Fig. 33.

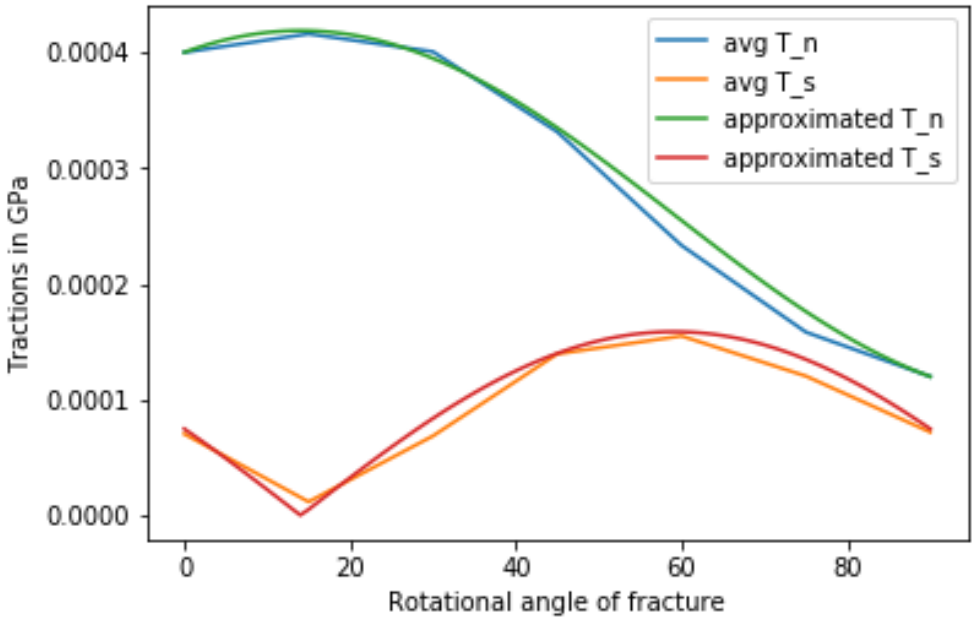

Figure 32: approximated vs numerical tractions for setup #1 with anisotropic BS

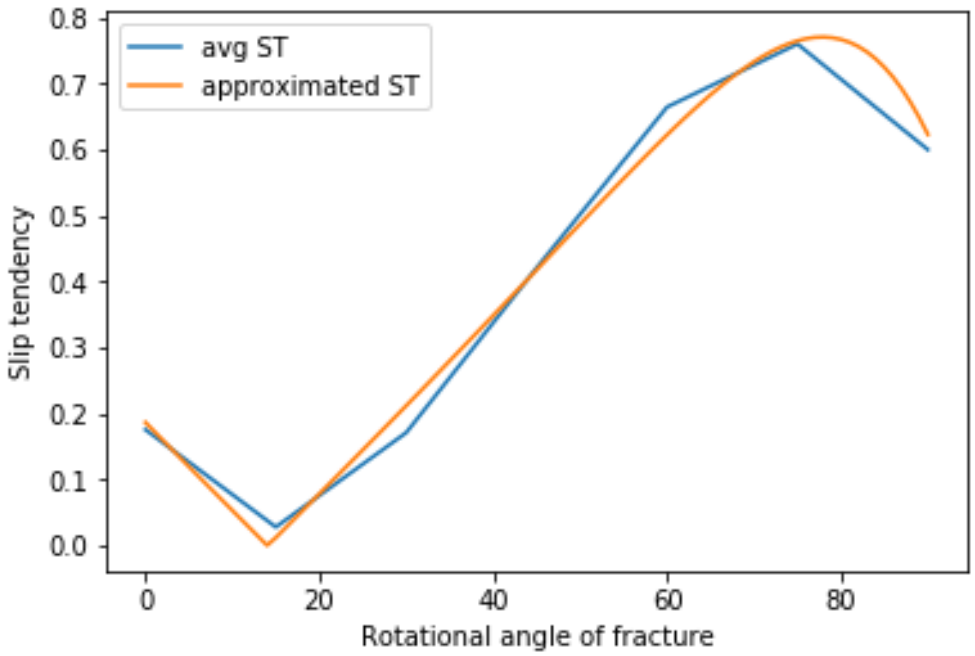

Figure 33: approximated vs numerical slip tendency for setup # 1 with anisotropic BS

As can be seen from Fig. 32 and Fig. 33, the approximated and numerical values match well.

Fig. 32 and Fig. 33 can be made sense of by the equations in the following way. As can be seen from Fig. 31 the normal tractions start at σ_{22} when the angle of the fracture is 0° since that is what σ_{22} is set to be. This correlates well with eq. (130) since $n_x = 0$ and $n_y = 1$ leaving only σ_{22} left in the equation. Likewise the normal traction drops down to σ_{11} at 90 due to $n_x = 1$ and $n_y = 0$. Now unlike the isotropic case which was symmetric around the angle of 45° where it increased before and decreased after. The normal tractions for the anisotropic case increases only up to 15° and then slightly decreases to 30° before it has a gradual drop until its minimum at 90°. The stress from the boundary conditions will affect the normal tractions in the same way as in the previous case, that is, an increase to the normal tractions before 45° followed by a decrease after. However, since σ_{11} is lower than σ_{22} the normal tractions due to the background stress will start decreasing as the fracture orients. The normal tractions gained from the boundary conditions will offset this fact until 15° so the net normal tractions will still be positive. However, after 15° the normal tractions due to the background stress will decrease more than the normal tractions due to the boundary conditions increases resulting in a drop in net normal tractions. The largest drop in normal tractions is seen to happen after 45° since then both the stress from the boundary conditions and the background stress will cause a decrease in normal tractions.
The shear tractions in Fig. 32 will also make sense following eq. (131).

5.3.3 Shear compression test with isotropic BS

The next simulation is very similar to the first simulation, except that the Dirichlet conditions on the top surface is set to be 1.5cm in a downward 45° direction, that is, $u_{0x} = 1.5$cm and $u_{0y} = -1.5$cm (setup # 2). Here again it is the same isotropic background stress $\sigma_{11} = \sigma_{22} = 0.12$MPa.

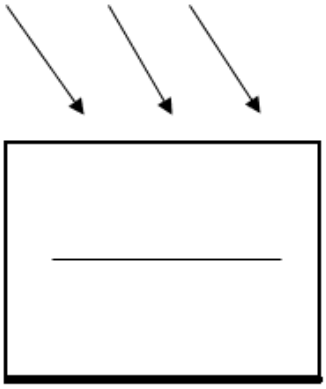

Figure 34: shear compression test 45° angle (Setup # 2) with isotropic BS

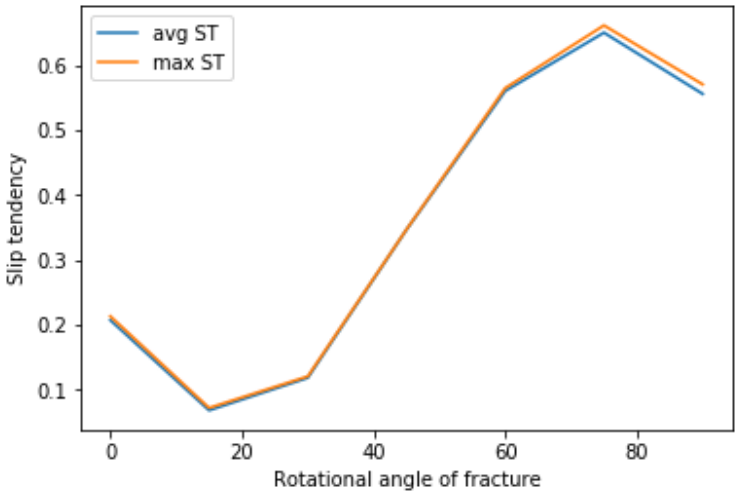

Figure 35: ST vs angle of the fracture for setup # 2 with isotropic BS

As can be seen from Fig. 35 the slip tendency will start slightly above 0.2 then take a dip to under 0.1 at 15 ° and slightly increase until 30° before it starts increasing quite rapidly afterwards. The fracture will begin to slip at about 70° where the slip tendency is 0.6 which is the threshold for slip to occur. The slip tendency is also seen to behave quite evenly on the whole fracture as seen from the small discrepancy between the average slip tendency and the maximum slip on the fracture. The test has very similar results to the

anisotropic shear case illustrated in Fig. 33. The reason being is that the internal stress due to the boundary conditions u_{0y} on this test is very similar to the background stress σ_{22} produced in the anisotropic shear case. The calculations done previously to explain the anisotropic shear case will therefore be a quite good approximation for this test.

Since the test is with an isotropic background stress the contribution from the background stress to the normal tractions will always be the same. To understand the behaviour of the normal traction, the only concern is then to understand the effects of the B.C's. The normal tractions can then be expressed as $T_n = T_n^{bc} + C$, where C is the constant value due to the background stress.
When the fracture is at 0° the normal tractions will be due to the B.C from u_{oy} and the background stress from σ_{22} while at 90° the only contribution is from the background stress σ_{11}.

The normal tractions will increase slightly from $0 - 30°$ since the contributions from u_{0x} will increase the tractions more than the slight decrease in the contribution from u_{0y}. However, after 30° the decrease from u_{0y} will be more than the increase from u_{0x}. After 45° is were the greatest drop in normal tractions occur, since at 45° is where the contributions from u_{0x} is at its highest. After this, both the contributions from u_{0x} and u_{0y} will keep diminishing.

The only concern for understanding the behaviour of the shear tractions is again only the stress contributions from the B.C's, since recalling that $T_s^{bs} = 0$ for the isotropic background stress. Understanding the shear tractions can be made by looking at the contributions from u_{0x} and u_{0y} in separated simulations and then taking a superposition of them. However, an accurate enough approximation was harder to come by. The shear tractions will decrease from $0-15°$ then increase from $15-60°$ before decreasing again from $60-90°$. The shear tractions will be equal at 0° and 90° since then the only contribution will be from u_{0x} which will have the same shear tractions as explained for the isotropic shear B.C case.

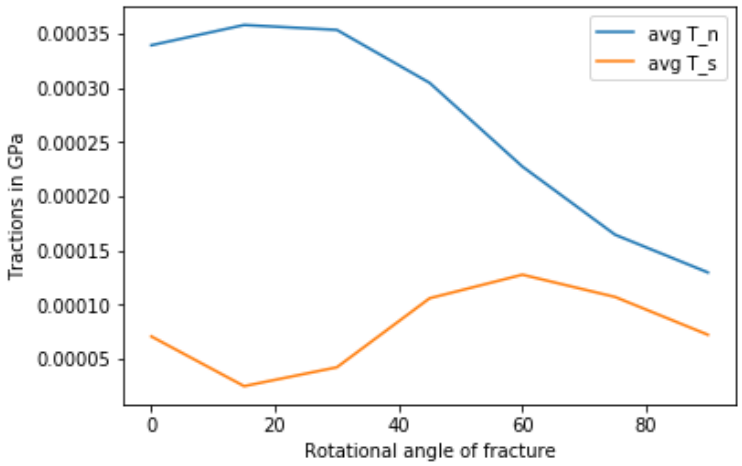

Figure 36: Traction vs angle of the fracture for setup # 2 with isotropic BS

5.3.4 Shear compression test with anisotropic BS

Now the same simulation will be done just with an anisotropic background stress, where $\sigma_{11} = 0.12$MPa and $\sigma_{22} = 0.4$ MPa.

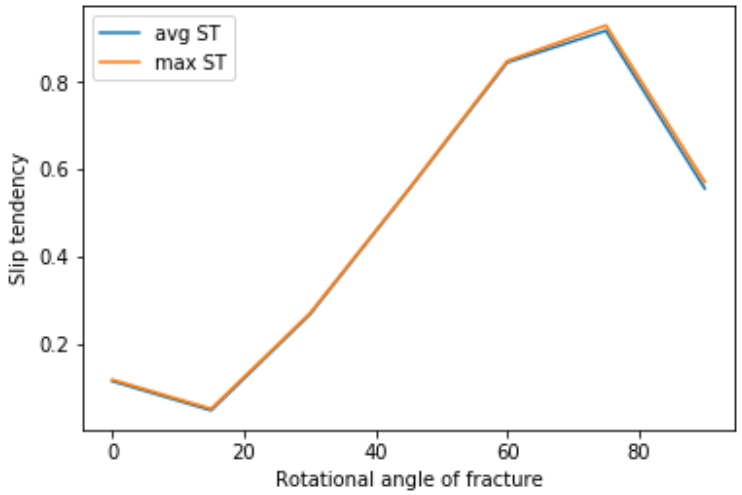

Figure 37: Slip tendency vs angle of the fracture for setup #2 with anisotropic BS

The slip tendency resembles the last simulation, since the only difference is the contributions from the background stresses. What is noteworthy is that the slip tendency is higher for the anisotropic case with about 0.2 compared to the isotropic case, and starts slipping after 45° when $ST \geq 0.6$. The reason being is that the anisotropy causes additional shear stress which increases the slip tendency.

The normal and shear tractions will behave according to the explanation given for the last test except that the contributions from the background stresses will be different and will be given by eq. (119) and eq. (120). This is shown in the following figure:

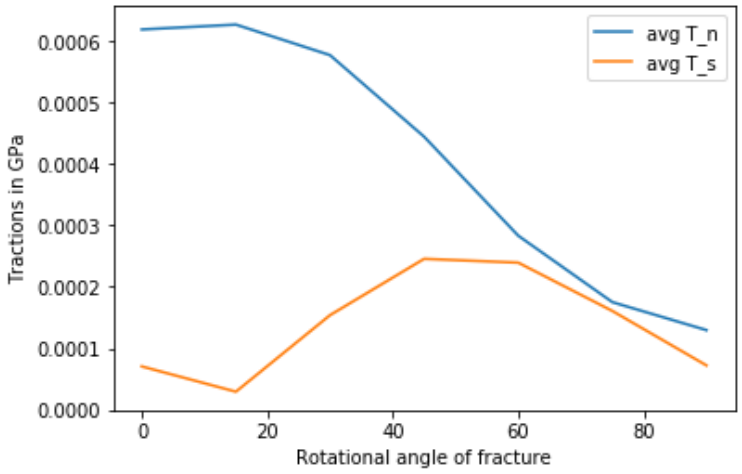

Figure 38: Traction vs angle of the fracture for setup # 2 with anisotropic BS

5.4 Slip tendency as a function of temperature

The next simulations will look at the slip tendency as a dependency on the temperature and will use the two types of boundary conditions used in the previous simulations. The angle for the rotation of the fracture will be based on the angle which caused the greatest degree of slip tendency in the previous simulations for the isotropic case. So for setup #2 the fracture will be set to an angle of 75 °. Similarly for setup #1 the fracture will be planar, representing an angle of 0°.

Before showing the simulations, some relationships between the slip tendency and temperature are needed. Recalling fig. 6 which showed the relationship between Young's modulus and temperature will in turn make the slip tendency dependent on temperature. This is due to the fact that the stress tensor for a homogeneous isotropic media depends indirectly on Young's modulus and can be expressed as equation (38) i.e

$$\boldsymbol{\sigma} = 2G\mathcal{E} + \lambda trace(\mathcal{E})I \tag{132}$$

where lame's parameters G and λ depends on Young's modulus, E by eq. (43) and eq. (44).

The stress will therefore decrease due to the fact that Young's modulus decreases with increasing temperatures, which in turn will make lame's parameters decrease.

The slip tendency will therefore also decrease with increasing temperatures, unless the normal stress decreases by the same amount or less than the shear stress.

In the following two simulations the temperature will go from 50℃ − 500℃. The first simulation will be with the shear B.C as explained earlier and with a planar fracture line (setup # 1).

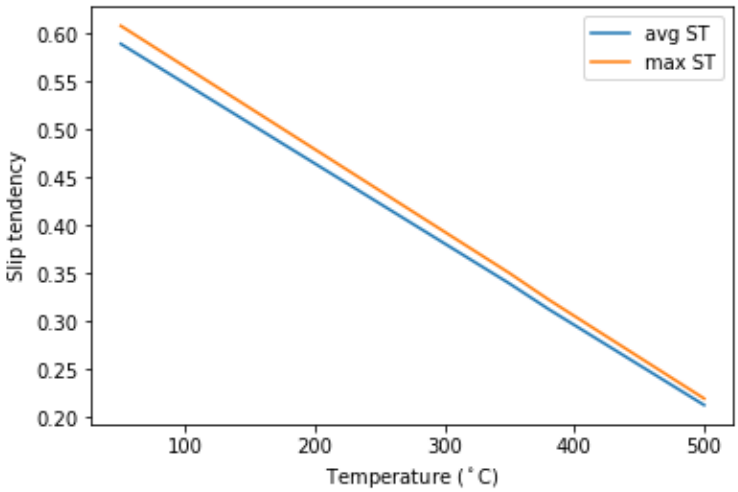

Figure 39: Slip tendency vs temperature for setup # 1 with isotropic BS

As can be seen from the figure, there is a linear decreasing relationship between the slip tendency and temperature. The slip tendency decreases quite significantly as well, taking a drop of almost 0.40. Starting at around the slip threshold of 0.60 at 50℃ and decreasing to under 0.25 at 500℃. This simulation clearly shows how much an effect the temperature can have on the slip tendency.

A decrease makes sense physically as the increase of temperature decreases the stresses following the logic explained earlier.

The second simulation uses setup #2 with an orientation of the fracture of 75°.

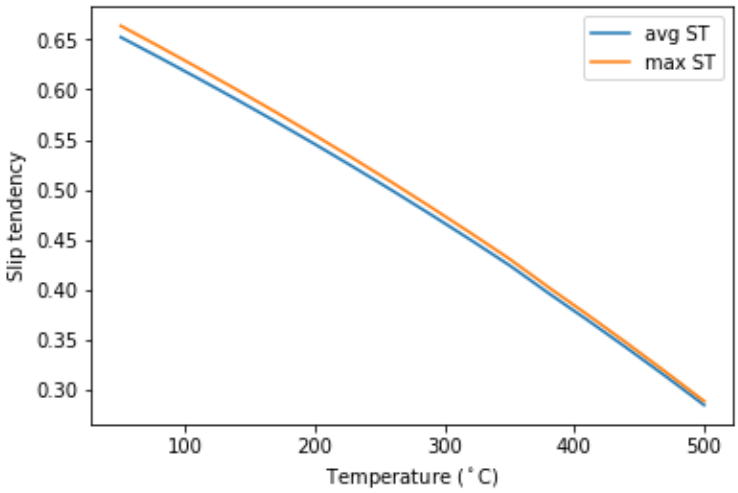

Figure 40: Slip tendency vs temperature with setup #2

As can be seen from the figure the relationship is not linear in this case, but the decrease in slip tendency is almost as great as in the previous example. Here the slip tendency drops 0.35, going from 0.65 at 50℃ to 0.30 at 500℃.

5.5 Slip tendency with a temperature gradient

So far, the focus has been on mechanical tests on the domain with the same tests done several times, but with constant temperatures. The next simulation will look at a mechanical test with a varying temperature and background stress gradient acting on the domain. The idea is to look at a more realistic geological condition.

The domain will now be $\Omega = [-16, 0]km \times [-16, 0]km$ and the fracture line is set to have an orientation of 75° being set to be $\Gamma = [\frac{-27500}{3}, \frac{-41500}{3}], [\frac{-20500}{3}, \frac{-6500}{3}]$km.

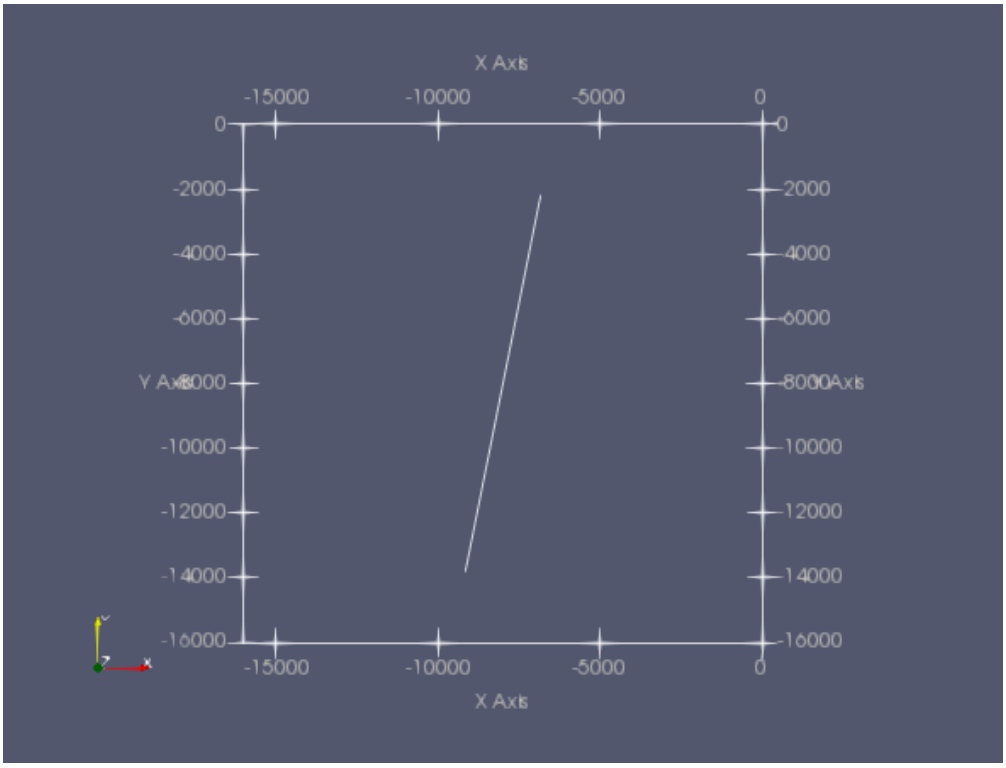

Figure 41: location of the fracture within the domain

Setup #2 is used, but the displacement values are changed in relation to the increase of the domain, so the displacement will be $u_{0x} = 8$cm and $u_{0y} = -8$cm. The background stress $\boldsymbol{\sigma}_{bs}$ and the temperature T increases with depth. The background stress is set to be $\sigma_{11} = \sigma_{22} = P_0 + \rho g y$ where y is measured in km according to [Ucar et al.2018a]. Here $g = 9.8\frac{m}{s^2}$ is gravity, $P_0 = 101325$Pa is the atmospheric pressure and ρ is the density of granite set to be $2750\frac{kg}{m^3}$ according to [Klein and Carmichael].

The temperature T is assumed to be increasing with depth y. The temperature is made to decrease by 30℃ per kilometer as in [Fridleifsson et al.2008] and set to be 20℃ at the surface.

$$T = 20 - 30y, \tag{133}$$

where $y \in [0, -16]$km is the depth of the domain.

Recalling the simulational values in the table (5) the same relationship between Young's modulus and the temperature based on these values has been used.

$$E = 40.37 - \frac{3}{56}T, \tag{134}$$

E will in turn be dependent on depth as can be seen by inserting eq. (133) into eq. (134)

$$E = 39.3 + \frac{45}{28}y. \tag{135}$$

For the test, T will be in the range of $T \in [50, 500]$℃, $E \in [13.6, 39.3]$ and $\boldsymbol{\sigma}_{bs} \in [0.10, 0.53]$MPa for the whole domain.

First a test will be done with a constant temperature of 20℃ contributing to a constant Young's modulus of $E = 39.3$. This is useful to be better able to compare the effects a temperature gradient will have on the next simulation.

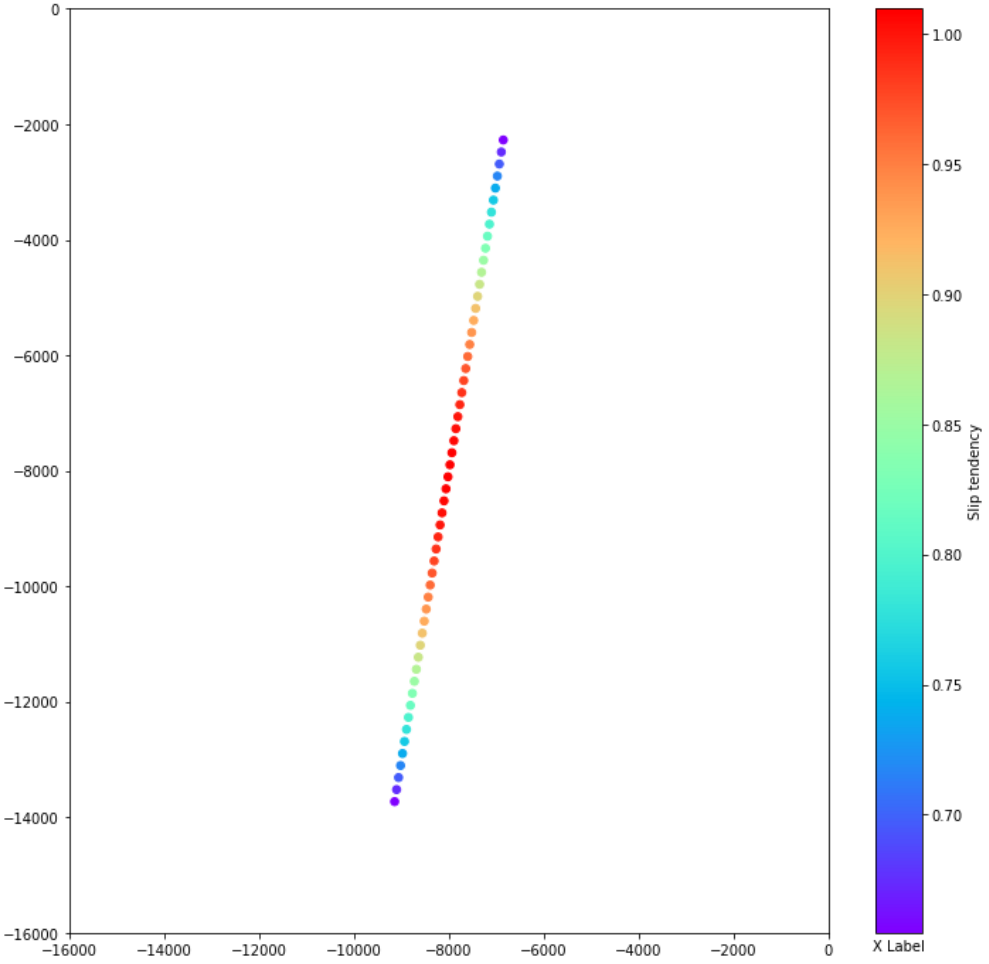

Figure 42: Slip tendency of a fracture with a constant temperature in the domain

Here the average slip tendency is 0.88, the minimum is 0.65 and the maximum is 1.

The second test is with the temperature gradient acting on the domain as explained above.

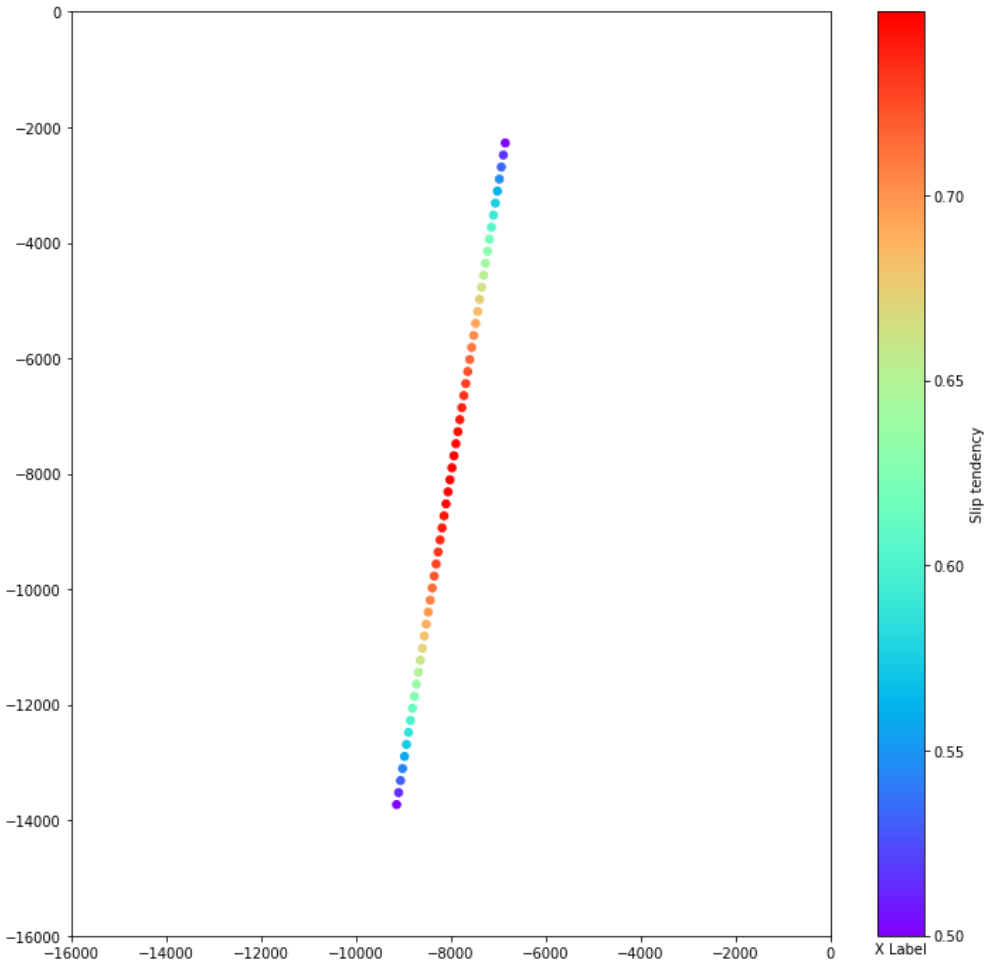

Figure 43: Slip tendency of a fracture with a temperature gradient acting on the domain

In this case the average slip tendency is 0.66, the minimum is 0.5 and the maximum is 0.75. As can be seen from Fig. 42 and Fig. 43 the slip tendency decreases on average with 0.22 from the simulation without a temperature gradient to the simulation with a temperature gradient. This is due to the far lower Young's modulus in the second test which will cause a reduced stress tensor. This will in turn cause a lower slip tendency as explained earlier.

In both simulations the slip tendency is lowest at the beginning and end, while highest near the center.

The background stress gradient influences to what extent the temperature gradient has an effect in the sense that the temperature will affect the slip tendency in a greater degree when the stress is higher, which will be the case further down into the domain due to the background stress gradient. The effect of the temperature gradient is more clearly seen in Fig. 44

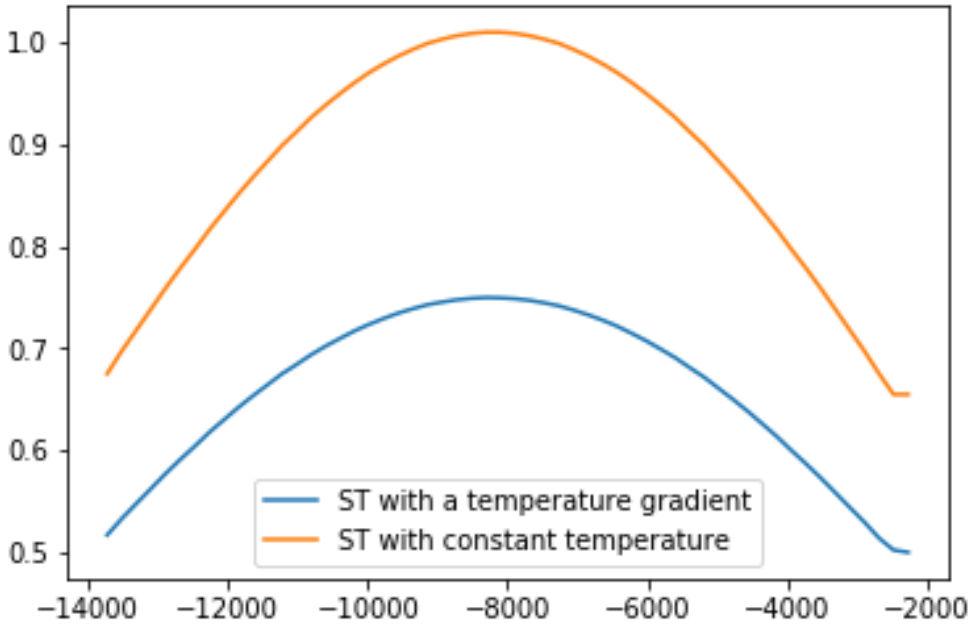

Figure 44: Slip tendency vs depth y comparing ST with a temperature gradient and without

As can be seen from Fig. 44 there is clearly a difference in the slip tendency with and without a temperature gradient and the highest difference in slip tendency between the two simulations is when the slip tendency is at its maximum value.

5.6 Slip tendency as a function of pressure

The next simulation will be a coupled mechanics and flow problem. The mechanics set up of the problem will be the same as setup # 2 and the domain $\Omega = [0, 3] \times [0, 3] km$, with the fracture $\Gamma = [\frac{4250}{3}, \frac{3250}{3}], [\frac{4750}{3}, \frac{5750}{3}]$km, oriented 75° in relation to the x-axis and with an aperture of $10cm$.

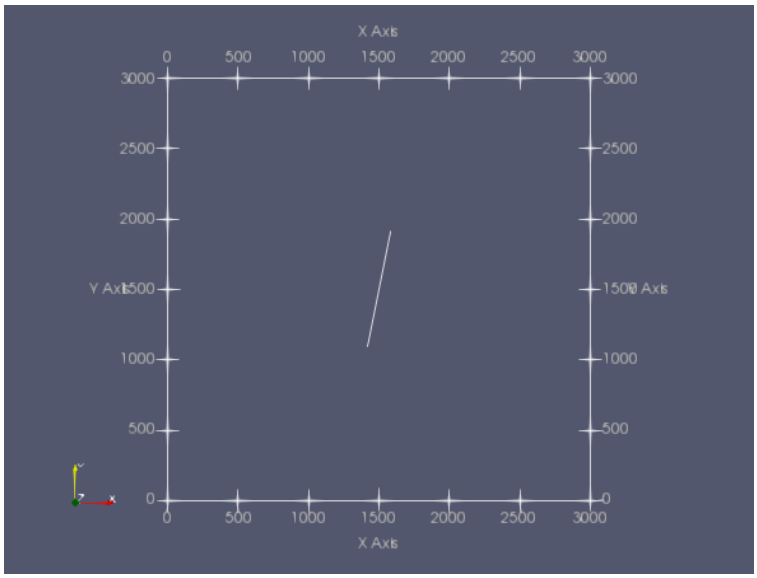

Figure 45: location of the fracture within the domain

The simulation for the mechanics problem is illustrated in Fig. 46

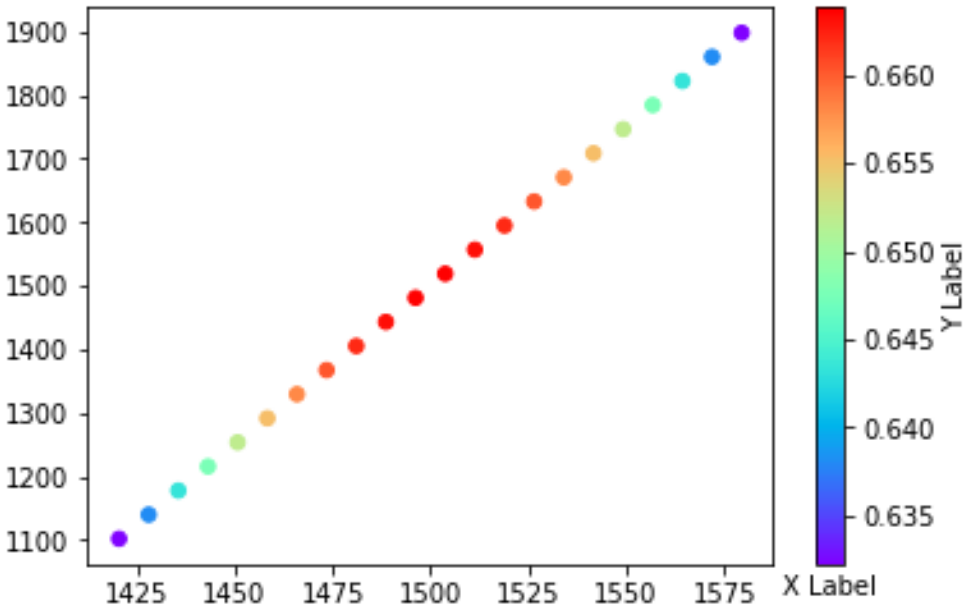

Figure 46: Slip tendency without a pressure gradient

For the flow problem Dirichlet conditions will be set on the top and bottom surfaces, while Neumann on the west and east side of the domain. A constant pressure will be set on the top surface, $P = 0.01$MPa and $P = 0$ at the bottom surface. The flux $\vec{q} = 0$ at the left and right surfaces as well, there will be no source within the domain. The permeability within

the domain is set to be $K = 1$ milli-Darcy (md) while the permeability within the fracture is set to be $K = 1000$md. Since the permeability within the fracture is much higher than the permeability within the matrix the flow will mostly go through the fracture resulting in a pressure gradient throughout the fracture.

The flow problem will be:

$$\begin{aligned} \nabla \cdot \vec{q} &= 0 \ \ in \ \ \Omega \\ \vec{q} &= -\boldsymbol{k}\nabla p \\ p_{|\partial\Omega_d} &= p_d \\ \vec{q}_{|\partial\Omega_n} &= \vec{q}_n \end{aligned} \tag{136}$$

coupled they become

$$-\nabla \cdot \boldsymbol{k}\nabla P = 0. \tag{137}$$

The MPFA method will solve the problem for the pressure, and the pressure gradient on the fracture is seen in Fig. 47

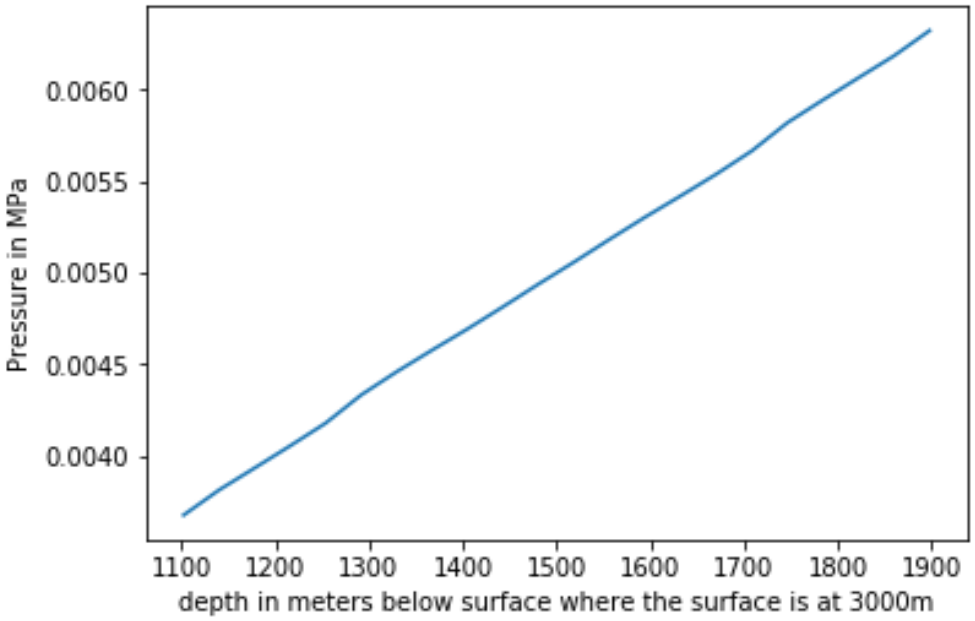

Figure 47: The pressure along the fracture

The normal tractions on the fracture will be different due to the pressure. The net effective normal traction will be $T_n^{eff} = T_n - p$ resulting in a different slip tendency as can be seen from Fig 48:

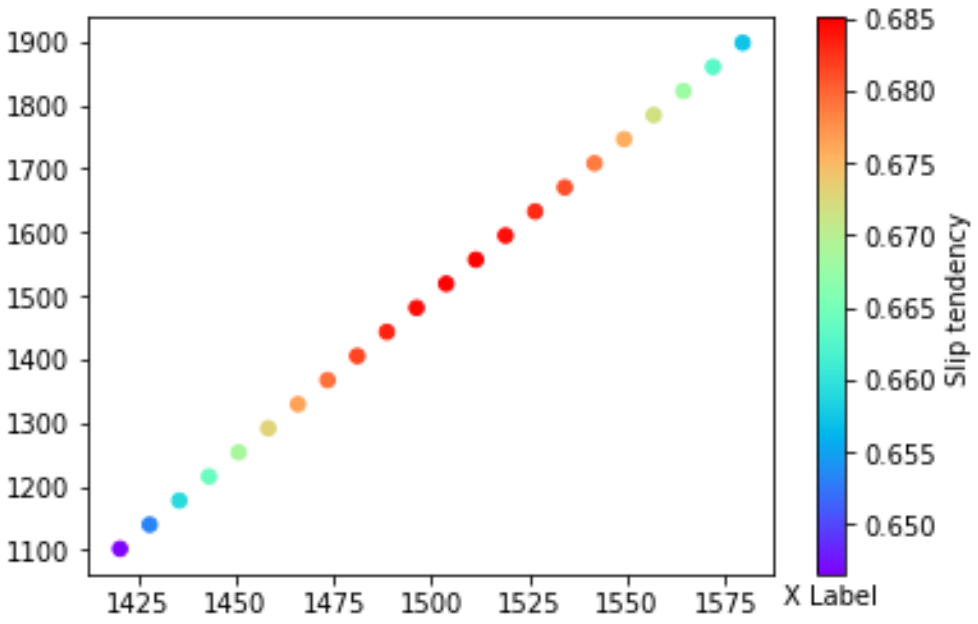

Figure 48: Slip tendency with a pressure gradient

Fig. 48 has generally the same symmetry as Fig. 46, that is, lower slip near the edges and higher slip closer to the center of the fracture. However, the slip tendency will on average be higher in Fig. 48 than in Fig. 46 due to the pressure contribution. Pressure will result in lower normal tractions since $T_n^{eff} = T_n - p$ which will result in higher slip tendency values. The slip tendency is also seen to be higher in Fig. 48 closer to the surface when $y = 1900$ and almost the same as Fig. 46 when $y = 1100$. This is due to the fact that pressure gradient is linearly decreasing with depth y, so higher closer to the surface and lower the further down as seen in Fig. 47. The effective normals tractions T_n^{eff} will therefore be lower closer to the surface resulting in a higher slip tendency.

The next example is a simulations of the slip tendency vs the pressure where the B.C pressure on the top surface will be $p_d \in [0.01, 0.1]$MPa with 0.009MPa increments.

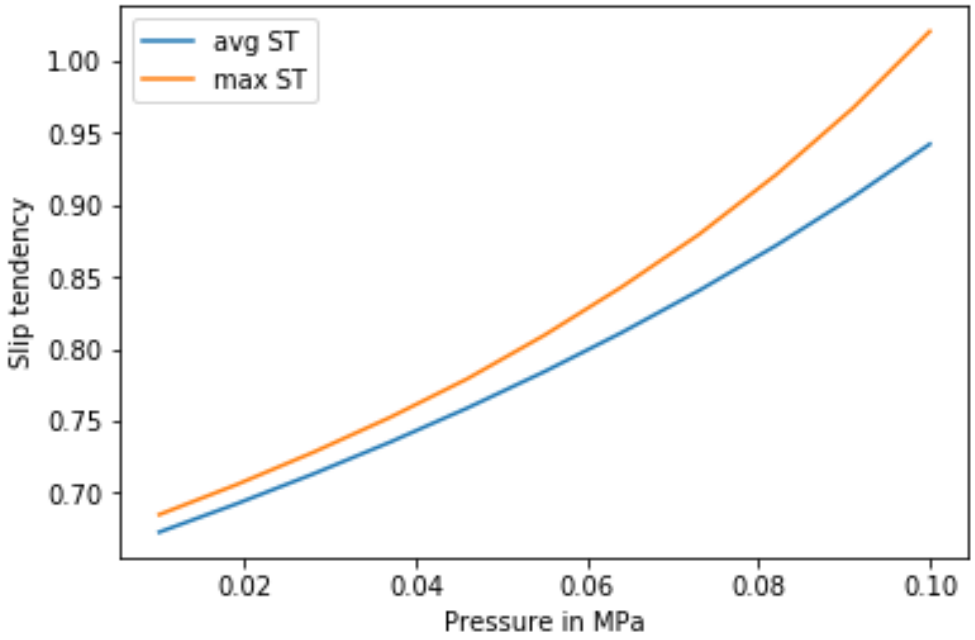

Figure 49: Slip tendency vs incremental pressure increases

As can be seen from Fig. 49 there is a direct correlation between the pressure increase and the slip tendency. As stated before, it is because the effective normal tractions T_n^{eff} decreases as the pressure increases resulting in higher slip tendency values. There is a gap between the average and maximum slip tendency, which increases as the pressure increases. This is due to the fact that the pressure gradient has varying pressures along the fracture resulting in some slip tendency values being higher than the average. There is a larger gap for higher pressure values since when the normal effective tractions T_n^{eff} are already low, a small fluctuation will cause a larger increase in the slip tendency.

6 Conclusion

At the beginning of the thesis the aims and objectives of the research was stated and as such a summary of the findings in relation to these objectives will be discussed. The first objective was to to increase understanding of temperature effects on thermally dependent rock parameters which has been accomplished through the study of elastic moduli and the relationship between Young's modulus E and temperature. It was also seen how the change in Young's modulus E affected the slip tendency in sec. 5.4. Throughout the simulations that were done, it was shown that temperature does in fact affect the slip tendencies, and to a far greater degree than what is often assumed in the literature. For instance the first simulation comparing the slip tendency with temperature showed a drop from 0.6 slip tendency at 50℃ to 0.20 at 500℃ which is a major change. The second objective was to provide more insight into flow and mechanics which was accomplished through the simulation in sec. 5.6 and showed that the coupling in terms of the slip tendency influenced only the normal tractions T_n. The final goal was to provide more insight into the relationship and correlation between temperature and slip tendency. This was accomplished through sec. 5.4 and sec. 5.5 where both sections showed simulations with a clear relationship between temperature and slip tendency. It was seen that the degree to which the slip tendency was affected by the temperature depended on the amount of stress within the domain, where a higher amount of stress caused the temperature to impact the slip tendency to a greater degree. Higher traction values was accomplished either through increasing the stress within the domain or through orientation of the fracture as in sec. 5.3.

Slip tendency analysis should start taking into account temperature effects, especially if there is a lot of temperature fluctuations in the domain for where the analysis is made, such as in geothermal reservoirs. Including temperature effects will provide better slip tendency predictions resulting in less unwanted fracture reactivations. This will mean that for geothermal reservoirs a more accurate prediction of how much fluid can be injected before a fracture will reactivate.

To get a full picture of temperature effects on the slip tendency a thermoelastic model which explains the formations in stress and displacement due to temperature should be introduced in the future. Modelling the heat transport for the fluid within the domain would also be an excellent additional contribution to get a better understanding of the temperature distribution within the domain.

References

[Aavatsmark2002] Aavatsmark, I. (2002). An introduction to multipoint flux approximations for quadrilateral grids. *Computational Geosciences*, 6(3):405–432.

[Aavatsmark2007] Aavatsmark, I. (2007). *Bevarelsesmetoder for elliptiske differensialligninger*. Universitetet i Bergen.

[Bower and Zyvoloski1997] Bower, K. M. and Zyvoloski, G. (1997). A numerical model for thermo-hydro-mechanical coupling in fractured rock. *International Journal of Rock Mechanics and Mining Sciences*, 34(8):1201 – 1211.

[Brotons et al.2013] Brotons, V., Tomás, R., Ivorra, S., and Alarcón, J. (2013). Temperature influence on the physical and mechanical properties of a porous rock: San julian's calcarenite.

[Fridleifsson et al.2008] Fridleifsson, I. B., Bertani, R., Huenges, E., Lund, J. W., Ragnarsson, A., and Rybach, L. (2008). The possible role and contribution of geothermal energy to the mitigation of climate change.

[Jaeger et al.2007] Jaeger, J., Cook, N., and Zimmerman, R. (2007). *Fundamentals of Rock Mechanics*. Blackwell.

[Keilegavlen et al.2017] Keilegavlen, E., Fumagalli, A., Berge, R., Stefansson, I., and Berre, I. (2017). Porepy: An open-source simulation tool for flow and transport in deformable fractured rocks.

[Keilegavlen and Nordbotten2017] Keilegavlen, E. and Nordbotten, J. M. (2017). Finite volume methods for elasticity with weak symmetry. *International Journal for Numerical Methods in Engineering*, 112(8):939–962.

[Kelkar et al.2014] Kelkar, S., Lewis, K., Karra, S., Zyvoloski, G., Rapaka, S., Viswanathan, H., Mishra, P. K., Chu, S., Coblentz, D., and Pawar, R. (2014). A simulator for modeling coupled thermo-hydro-mechanical processes in subsurface geological media. *International Journal of Rock Mechanics and Mining Sciences*, 70:569 – 580.

[Khalili and Selvadurai2003] Khalili, N. and Selvadurai, A. P. S. (2003). A fully coupled constitutive model for thermo-hydro-mechanical analysis in elastic media with double porosity. *Geophysical Research Letters*, 30(24).

[Klein and Carmichael] Klein, C. and Carmichael, R. S. rock.

[Liu and Xu2015] Liu, S. and Xu, J. (2015). An experimental study on the physico-mechanical properties of two post-high-temperature rocks. *Engineering Geology*, 185:63 – 70.

[Lockner et al.1986] Lockner, D. A., Summers, R., and Byerlee, J. D. (1986). Effects of temperature and sliding rate on frictional strength of granite. *pure and applied geophysics*, 124(3):445–469.

[Moeck et al.2009] Moeck, I., Kwiatek, G., and Zimmermann, G. (2009). Slip tendency analysis, fault reactivation potential and induced seismicity in a deep geothermal reservoir. *Journal of Structural Geology*, 31(10):1174 – 1182.

[Morris et al.1996] Morris, A., Ferrill, D., and Henderson, D. B. (1996). Slip-tendency analysis and fault reactivation.

[Neves et al.2009] Neves, M. C., Paiva, L. T., and Luis, J. (2009). Software for slip-tendency analysis in 3d: A plug-in for coulomb. *Computers Geosciences*, 35(12):2345 – 2352.

[Nordbotten2014] Nordbotten, J. M. (2014). Cell-centered finite volume discretizations for deformable porous media. *International Journal for Numerical Methods in Engineering*, 100(6):399–418.

[Nordbotten and Celia2012] Nordbotten, J. M. and Celia, M. (2012). *Geological storage of* $CO_2 modelingapproachesforlarge - scalesimulation. Wiley.$

[Pouzada et al.2006] Pouzada, A. S., Ferreira, E. C., and Pontes, A. J. (2006). Friction properties of moulding thermoplastics. *Polymer Testing*, 25(8):1017 – 1023.

[Salimzadeh et al.2018] Salimzadeh, S., Paluszny, A., Nick, H. M., and Zimmerman, R. W. (2018). A three-dimensional coupled thermo-hydro-mechanical model for deformable fractured geothermal systems. *Geothermics*, 71:212 – 224.

[Sibson1985] Sibson, R. H. (1985). A note on fault reactivation. *Journal of Structural Geology*, 7(6):751 – 754.

[Stesky1975] Stesky, R. (1975). the mechanical behavior of faulted rock at high temperature and pressure.

[Stesky1978] Stesky, R. M. (1978). Rock friction-effect of confining pressure, temperature, and pore pressure. *pure and applied geophysics*, 116(4):690–704.

[Sygała et al.2013] Sygała, A., Bukowska, M., and Janoszek, T. (2013). High temperature versus geomechanical parameters of selected rocks – the present state of research. *Journal of Sustainable Mining*, 12(4):45 – 51.

[Tadmor et al.2011] Tadmor, E., Miller, R., and Elliott, R. (2011). *Continuum Mechanics and Thermodynamics:From Fundamental Concepts to Governing Equations*. Cambridge University Press.

[Tian et al.2017] Tian, H., Mei, G., Guo-sheng, J., and Qin, Y. (2017). High-temperature influence on mechanical properties of diorite. *Rock Mechanics and Rock Engineering*, 50(6):1661–1666. Copyright - Rock Mechanics and Rock Engineering is a copyright of Springer, 2017; Last updated - 2017-05-27.

[Ucar et al.2018a] Ucar, E., Berre, I., and Keilegavlen, E. (2018a). Three-dimensional numerical modeling of shear stimulation of fractured reservoirs. *Journal of Geophysical Research: Solid Earth*, 123(5):3891–3908.

[Ucar et al.2018b] Ucar, E., Keilegavlen, E., Berre, I., and Nordbotten, J. M. (2018b). A finite-volume discretization for deformation of fractured media. *Computational Geosciences*, 22(4):993–1007.

[Watanabe et al.2009] Watanabe, N., Wang, W., McDermott, C. I., Taniguchi, T., and Kolditz, O. (2009). Uncertainty analysis of thermo-hydro-mechanical coupled processes in heterogeneous porous media. *Computational Mechanics*, 45(4):263.

[Weizhong et al.2009] Weizhong, C., Xianjun, T., Hongdan, Y., Guojun, W., and Shanpo, J. (2009). A fully coupled thermo-hydro-mechanical model for unsaturated porous media. *Journal of Rock Mechanics and Geotechnical Engineering*, 1(1):31 – 40.

[Worum et al.2004] Worum, G., van Wees, J., Bada, G., van Balen, R. T., Cloetingh, S., and Pagnier, H. (2004). Slip tendency analysis as a tool to constrain fault reactivation: A numerical approach applied to three-dimensional fault models in the roer valley rift system (southeast netherlands). *Journal of Geophysical Research: Solid Earth*, 109(B2).

[Zhang et al.2009] Zhang, L., XianBiao, M., and AiHong, L. (2009). Experimental study on the mechanical properties of rocks at high temperature. *Science in China Series E: Technological Sciences*, 52(3):641–646.